^{185}W(n,γ) Cross-sections Constrained with Statistical Nuclear Properties of ^{186}W nucleus

by

Mvuyisi Mbabane

Thesis presented in partial fulfilment of the requirements for the degree of Masters in Physics at University of Johannesburg

Supervisors:

Dr. B.V. Kheswa

University of Johannesburg and iThemba LABS

Dr. P. Masiteng

University of Johannesburg

November 2018

Abstract

At some locations along the s-process reaction path, there exists nuclei with β-decay rates that competes with the neutron capture rates. Leading to a new possibility in s-process path because the radioactive nucleus may capture a neutron instead of undergoing the expected β decay. As a result the s-process is split into two to account for neutron capture possibility. The nuclei at which this occur are are known as s-process branch-point nuclei, which are worth looking into because they can be used to estimate stellar temperature and neutron density at the s-process site. However studying has proven to be a challenge since their (n, γ) cross section are usually not measurable by direct measurements. One of these branch-point nuclei is ^{185}W, and is important due to the Re-Os cosmochronology whereby the ^{187}Re –^{187}Os pair may be used as a chronometer to estimate stellar nucleosynthesis duration in the universe before the formation our solar system. However, the existence of branch point nuclei at leads to inconclusive analysis. Hence the need for better constraints of their (n, γ) cross-sections. In this work the nuclear level density and γ strength function of ^{186,187}W were measured with th Oslo method using ^{186}W(d, d') and ^{186}W(d, d') reactions. These new experimental data were successfully used to constrain ^{185}W(n, γ) cross sections within the Hauser-Feshbach model.

Declaration

I, Mvuyisi Mbabane, student number 201705941, University of Johannesburg, do solemnly declare that this report entitled "^{185}W(n,γ) Cross-sections Constrained with Statistical Nuclear Properties of ^{186}W nucleus" is original and a direct result of my own efforts. I personally undertook it with the professional guidance of my supervisors whose names and signatures appear below. All sources used in the study have been indicated and acknowledged by way of complete references.

Student: Mr M Mbabane	Date
Supervisor: Dr B.V. Kheswa	Date
Co-supervisor: Dr L.P. Masiteng	Date

Dedication

This work is dedicated to my family

Acknowledgements

I would like to give thousands of thanks to my supervisor Dr. Bonginkosi Kheswa. His continuous support financially and academically, his patience, motivation and expertise has guided me through this work. I would also like to thank my co-supervisor Dr. Paulus Masiteng for being there when I had no hope financially, for his input and personal encouragement during this research. I am extremely grateful to iThemba LABS and NRF for funding my studies, I would have been hopeless without their support. Lastly I am grateful for University of Johannesburg for allowing me an opportunity to enroll at such prestigious institution.

Contents

List of Figures

Chapter 1

Introduction

According to the Big Bang model, the universe which is made up of many galaxies, was created approximately 14 billion years ago by the big bang. This model is not clear of what happened before the big bang, but there are theories for nuclear reactions that occurred after it and up to the present day. These theories were made to try to explain the observed elemental abundances. Less than 1 second after the Big Bang, the average thermal energy was so high ($>$ 1MeV) that the protons converted to neutrons and vice versa, through e^- and e^+ capture reactions and were indistinguishable [1]. After 2 s the universe expanded further, cooling down to thermal energies $<$ 1 MeV. At these temperatures the protons and neutrons were able to retain their identities and combined to form light elements like hydrogen, helium and trace amount of Beryllium and lithium. This process is called primordial nucleosynthesis and took place within a period of 250 s. The most dominant reactions of the primodial nucleosythesis are illustrated in figure 1.1.

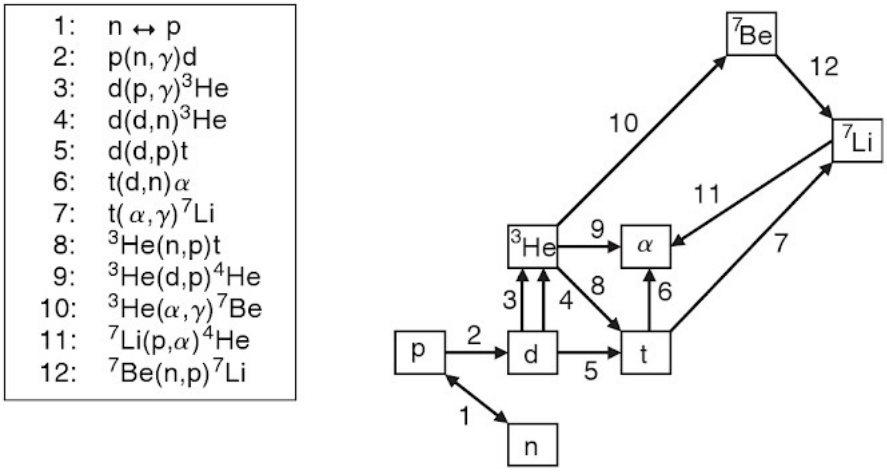

Figure 1.1: The reaction chain for formation of first elements [1].

After this period thermal energies decreased to ~ 0.1 MeV and the primordial reactions stopped. The unstable nuclei decayed by weak interactions, leaving the universe consisting of only protons, deuterons, ^{3}He, ^{4}He, e^-, γ-rays and neutrinos. The atomic era started 380000 years later where temperatures were approximately 10^3 K and electrons could remain bound in atoms [1]. The stars and galaxies were formed after billion years, by gravitational attraction. Some stars collapsed, giving birth to all new kinds of reactions which still take place even today.

1.1 Motivation and Objectives

A star may undergo different burning cycles producing elements mainly by fusion up to iron [2]. After the formation of iron, fusion ceases and there is not any energy produced to balance the gravitational force pulling star inwards, as a result the star dies. Clearly there must be some other processes responsible for the observed elemental abundance of nuclei heavier than iron. Burbidge and Fowler [3] were the first to suggest that these heavy nuclei are

mostly produced through neutron capture. The neutron capture occurs mainly by two processes namely slow neutron capture (s-process) and rapid neutron capture (r-process), additionally, there exist other processes responsible for a small number of nuclei which occur by neither of the aforementioned processes. These processes are rapid proton capture (rp-process), photodisintegration (p-process) and neutrino capture(υ-process), figure 1.2 shows paths of s-, r-, rp-,p-process in the nuclear chart.

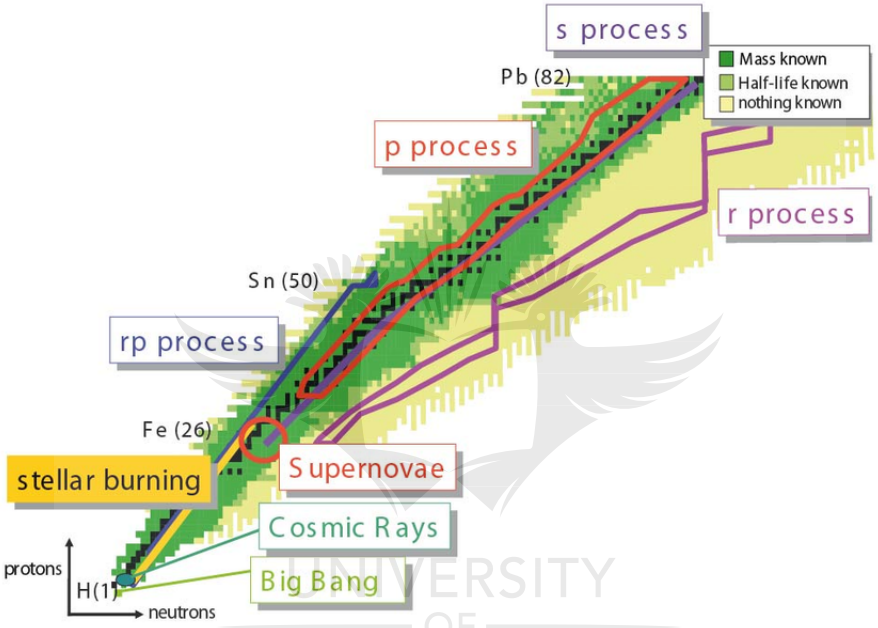

Figure 1.2: Illustration of s-, r-, rp and p-process paths along the nuclear chart [4].

However this work focuses on s-process only, therefore, the other processes will not be discussed any further. The s-process occurs by a series of neutron captures by a nucleus forming isotopes until an unstable isotope is reached. The unstable Isotope usually does not capture any further neutrons since neutron capture is usually very slow compared to β-decay rate. The isotope typically β decay to the next stable isobar, thus the s-process path follows the valley of

stability. However there are special cases where an unstable nucleus has neutron capture rate and β-decay rate that are comparable in magnitude. Thus, this nucleus can survive long enough to capture a neutron before β-decaying, and this splits the s-process path. Such nuclei are called branch-point nuclei, and are very important because they can be used for various applications such as constraining astrophysical conditions (stellar temperature and neutron density) in the asymptotic giant branch stars [5]. However, such analysis require reliable experimental neutron capture cross sections of these branch point nuclei. On the other hand they are problematic because they usually not easily accessible with direct measurements such as neutron time-of-flight (n-TOF) method due to their radioactive nature, which makes it impossible to make the target material, although recent experimental improvements have shown some promise in this respect [6]. There is certainly a critical need for further experimental constraints on the branch-point nuclei.

Three of such branch point nuclei are ^{185}W, ^{186}Re, and ^{186}Os, are of important because of the so-called Re-Os cosmochronology whereby the ^{187}Re- ^{187}Os parent to daughter ratio may be used to estimate the stellar nucleosynthesis duration that occurred prior the formation of our solar system [7]. This chronometer works by comparing abundances of parent(Re) with the daughter(Os) nucleus. The basic idea is to see how much ^{187}Re has decayed into ^{187}Os. However ^{187}Os is also made through s-process, therefore to find contribution from Os decay, the s-process must be subtracted and only then the Re-Os can be used for estimation [8]. However, the existence of s-process branch points at ^{185}W and ^{186}Re [9] induces complications. Hence, the necessity for determining the (n, γ) cross section of these nuclei. This work focuses on only one branch point nucleus, ^{185}W. Although the (n, γ) cross section is virtually inaccessible by direct measurements on ^{185}W due to unstable target nucleus, the compound nucleus following neutron capture, ie ^{186}W is certainly

reachable in stable beam experiments. Thus, its average statistical properties, i.e. the nuclear level density and γ-strength function, can be measured through the Oslo method [10], and the cross section be inferred by means of statistical calculations within the Hauser-Feshbach formalism [11] implemented in the TALYS open-access reaction code [12].

The main goal of this study is to constrain the (n, γ) cross sections of ^{185}W using the nuclear level densities and γ strength functions of the corresponding compound nucleus ^{186}W. The relationship between neighboring isotopes (in this case from ^{187}W compound nucleus) will be used to deduce ^{186}W properties, since some of its input parameters are not available. Additionally ^{187}W compound nucleus was used to calculate $^{186}\mathrm{W}(n, \gamma)$ cross sections and benchmark the method, since there are various experimental data of $^{186}\mathrm{W}(n, \gamma)$ reaction available. In particular, the objectives of this study were to (i) extract the nuclear level density and γ strength functions of ^{186,187}W nuclei from particle-γ coincidences, which were obtained using $^{186}\mathrm{W}(d, d')$ and $^{186}\mathrm{W}(d, p)$ reactions respectively, and (ii) use these experimental γ strength functions and nuclear level densities to calculate the $^{185}\mathrm{W}(n, \gamma)$ and $^{186}\mathrm{W}(n, \gamma)$ cross-sections in the Hauser-Feshbach formalism.

Chapter 2

Literature Review and Theory

2.1 Statistical Nuclear Decay Properties

Nuclear reactions can excite nuclei through single particle excitation and collective excitation, such as monopole vibration and rotation of oblate and prolate nuclei. As the nuclear excitation energy approaches the neutron separation energy, the number of quantum states increase exponentially and their width also increases. This excitation energy region is known as a quasicontinuum region. Such energy levels are unresolvable with the current experimental resolution. Hence they cannot be individually used to investigate nuclear properties, such as excitation energy, spin and parity. As a result, nuclear decay properties in the quasicontinuum region are best described using two statistical quantities which are nuclear level density and γ strength function. These are discussed in details below.

2.1.1 Nuclear Level Density

Nuclear level density (NLD) refers to the number of energy levels in a unit of excitation energy. There are numerous theoretical models for prediction of the nuclear level density but only the Back-Shifted Fermi gas (BSFG) and

constant temperature (CT) models were adopted in this work because of their simplicity. The BSFG model was proposed by Gilbert and Cameron in 1965, as a refinement to the Bethe's fermi gas model. According to original fermi gas model, a nucleus is gas of non interacting fermions confined inside a potential. In this model, the level density function for an excitation energy E_x is given by [13]

$$\rho(E_x) = \frac{\sqrt{\pi}}{12} \frac{\exp\left(2\sqrt{aE_x}\right)}{a^{1/4}E_x^{5/4}} \ , \tag{2.1}$$

where the level density parameter a is calculated by

$$a = \frac{\pi}{6}(g_p + g_n), \tag{2.2}$$

and g_p and g_n are proton and neutron single level density parameters, respectively. The Gilbert and Cameron refined equation 2.1 to account for pairing correlations, collective phenomena and shell effects by introducing free parameters that can be altered to fit the experimental data on level spacings obtained from neutron and resonance experiments. They proposed a nuclear level density that is given by [14]

$$\rho(E_x) = \frac{\sqrt{\pi}}{12} \frac{e^{(2\sqrt{aU})}}{a^{1/4}U^{5/4}} \frac{1}{\sqrt{2\pi\sigma}} \ , \tag{2.3}$$

where the U is the back shifted energy ,$U = E_x - \Delta_p - \Delta_n$, where Δ_p and Δ_n represents proton and neutron pairing energies, respectively. The spin cutoff σ is given by

$$\sigma^2 = g\langle m^2 \rangle T, \tag{2.4}$$

where $g = g_p + g_n$ and $\langle m^2 \rangle$ is the mean square number for single particle states. The temperature T is approximated by

$$T = \sqrt{U/a}. \tag{2.5}$$

Another model that was used in this work is a constant temperature model. This model is only applicable at $E_x < 10$ MeV [14]. It assumes a nearly constant temperature for all J^π and its level density is calculated by

$$\rho(E_x) = \frac{1}{T} e^{\frac{E_x - E_0}{T}} \tag{2.6}$$

where the free parameters T and E_0 are the nuclear temperature and energy-shift parameter, respectively, and have to be fitted to measurements of nuclear level density.

2.1.2 γ-Strength Function

The γ strength function (γ-SF) is the measure of average electromagnetic properties of nuclear transitions in the quasi-continuum. The transition can either occur through photo-absorption from a low energy to excited energy states or γ-decay from excited states interval to lower energy states. The γ strength functions corresponding to these modes of transitions are referred to as upward and downward strength functions respectively. However this work focuses on the latter and it is referred to as γ-strength function. For simplicity in notation, it is denoted as $f(E_\gamma)$. According to Ref.[15], the radiative strength function of a nuclear decay from a states with energy E_i to a lower energy E_f state, with electromagnetic character X and multi-polarity L, is calculated by

$$f_{XL}(E_\gamma) = \frac{\langle \Gamma_{\gamma l} \rangle}{D_l E_\gamma^{2L+1}} \tag{2.7}$$

where $\langle \Gamma_{\gamma l} \rangle$ and D_l are the average partial radiative width, level spacing of the initial states. $f(E_\gamma)$ is measured with model-dependent experimental methods (which means you have to rely on the model to extract it from experimental data). However there exist theoretical models with which it can be calculated when experimental data is unknown. Such models can also be fitted to known data and used to extrapolate the experimental $f(E_\gamma)$ to various energy regions. However, none of those models were used in the present work and therefore they will be omitted because they do not affect the final cross section results and their description is found in [27; 28].

2.2 The Oslo Method

The Oslo Method is an experimental technique that relies models for simultaneous extraction of NLD and γ-SF from particle-γ coincidence data. It was developed University of Oslo in the 1980s by the nuclear physics group. Its basic idea was to remove all strip the data for other contributions and leave only information relating to the reaction. It is made up by the following major steps: (i) unfolding of γ-ray spectra, (ii) first generation method and (iii) extraction and normalization of level density and transmission coefficient [10].

2.2.1 Unfolding of γ-ray spectra

As discussed in Section 3.3.2, there are three major processes in which γ rays interact with detector material namely, photoelectric effect, Compton scattering and pair production. Ideally all γ-rays would be fully absorbed in a detector and the observed spectrum would comprise only full energy peaks of the detected γ rays. This is not the case in real experiments. The measured γ

ray spectra consist of the contribution from all three processes. However, the Oslo method can only be applied on spectra that consist of the true full energy peaks. Thus, the experimental spectra must be unfolded to remove Compton background. This is achieved using the iterative procedure called unfolding method [16] and it is discussed below.

The unfolding procedure relies on experimentally measured detector response functions. These functions predict the percentage of Compton background at a given channel for every incident γ ray energy. In principle they should be measured for every possible γ ray energy but this is impossible. Thus, for NaI(Tl) detectors used in this project, they were measured for ten mono-energetic γ rays in the energy range 122 - 15110 keV [16]. These are interpolated to obtain the detector response functions for all other energies. In particular, the Compton background is interpolated between channels with the same γ ray scattering angles as shown in figure 2.1.

The single escape, double escape, annihilation and full energy peaks are interpolated by fitting the Gaussian distribution at interpolated energies. The width of the interpolated peaks is obtained by adjusting the standard deviation such that the experimental resolution is reproduced. Once the detector response functions are interpolated, they are used to construct the response matrix $\mathbf{R}$ with elements R_{ij} which are the response in channel i due to a γ ray energy from channel j. The response matrix is normalized such that

$$\sum_i R_{ij} = 1 \ . \tag{2.8}$$

The unfolded spectrum, u, is obtained using f = Ru which is equivalent to

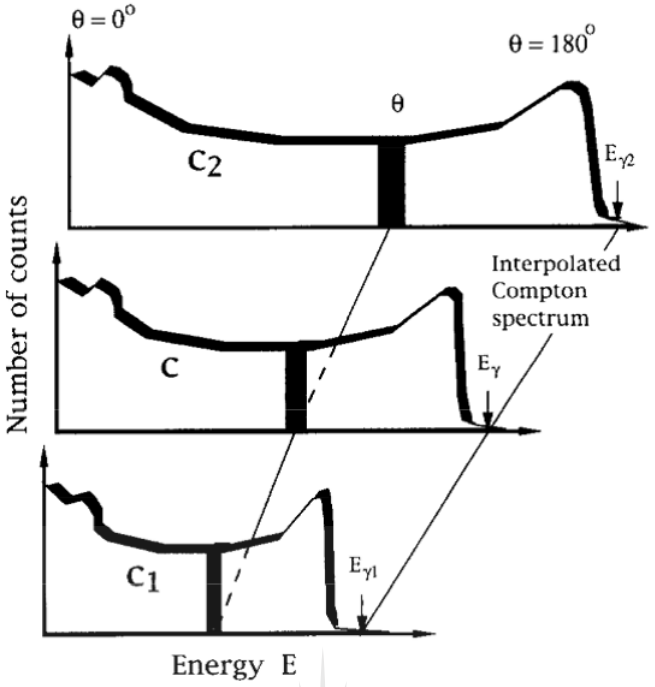

Figure 2.1: Compton interpolation from measured detector response functions c_1 and c_2, where c is the interpolated detector response function [16].

$$\begin{pmatrix} f_1 \\ f_2 \\ \vdots \\ f_N \end{pmatrix} = \begin{pmatrix} R_{11} & R_{12} & \dots & R_{1N} \\ R_{21} & R_{22} & \dots & R_{2N} \\ \vdots & \vdots & \ddots & \vdots \\ R_{N1} & R_{N2} & \dots & R_{NN} \end{pmatrix} \begin{pmatrix} u_1 \\ u_2 \\ \vdots \\ u_N \end{pmatrix},$$

where f and $\mathbf{R}$ are folded spectrum and response matrix, respectively. In particular, the unfolded spectrum is guessed, folded, compared to the measure raw spectrum r and improved until the folded spectrum is exactly the same as r. This is achieved iteratively using following steps:

1) Let the first trial unfolded spectrum u^0 equal to the measured spectrum r: $u^0 = r$

2) Fold u^0 according to $f^0 = Ru^0$

3) Calculate the difference spectrum $r - f^0$

4) Add the difference spectrum to the first unfolded one u^0 and obtain the next trial spectrum $u^1 = u^0 + r - f^0$

5) Fold u^1 and obtain a new folded spectrum f^1 according to $f^1 = Ru^1$

6) Continue using $u^i = u^{i-1} + (r - f^{i-1})$ to find the trial spectra and folding them until $f^i \approx r$, where i represent the ith iteration.

The unfolded spectrum u_i, is used to calculate the exact contributions from full energy (photoelectric effect) u_f, single escape u_s, double escape u_d, annihilation u_a and Compton scattering to the original observed spectrum. These are subtracted from the raw spectrum, at every channel i, to get the unfolded full-energy spectrum. This process begins by recognizing that for every channel i the measured γ spectrum can be written as $r(i) = p_f(i)u(i) + p_s(i)u(i) + p_d(i)u(i) + p_a(i)u(i) + c(i)$. The coefficients $p_f(i)$, $p_s(i)$, $p_d(i)$, $p_a(i)$ are probability of an event in channel i as a result of full energy absorption, single escape, double escape and annihilation, respectively. The values of these probabilities are obtained from Ref. [16].

Thus the unfolded spectrum of full energy peaks is given by: $u_f(i) = (r(i) - p_s(i)u(i) - p_d(i)u(i) - p_a(i)u(i) - c(i))/p_f(i)$. This is the spectrum from which the unfolded excitation energy E_x vs γ ray energy matrix is constructed, after correcting for detector efficiency.

2.2.2 First generation method

The extraction of NLD and γ-SF requires knowledge of the first generation (primary) γ spectra for all E_x of the nucleus in question. These are obtained using the iterative procedure called first generation method [17]. In this technique it is assumed that states populated through nuclear reactions have same decay properties as states populated by γ decay at that E_x, and ii) fact that

the γ spectra f_i from an E_x bin i of an unfolded particle-γ coincidence matrix, has all generations of γ rays from all possible decay cascades. Thus the primary γ-rays of each excitation energy bin is obtained using $h_i = f_i - g_i$ where g_i is the weighted sum of all spectra of lower excitation energy bins j < i and is given by $g_i = \sum_j b_{ij} w_{ij} f_j$. The coefficient b_{ij} is the correction factor for different cross-sections of populating states in bin i and lower energy levels in bins j. It is calculated from the ratio

$$b_{ij} = \frac{S_j}{S_i} \tag{2.9}$$

where S_j and S_i are number of states populated in bins j and i respectively. The number of populated states in found using the E_x spectrum. The weighting factor w_{ij} represents the probability of having decays between bin i to bin j, and the sum of w_{ij} over all j is unity. Thus the distributions of w_{ij} and h_i are exactly the same. This relationship is used to find h_{ij} and w_{ij} simultaneously using following iterative algorithm.

1) Apply a trial function for w_{ij}.

2) Compute h_i from from $h_{ij} = f_i - g_j$.

3) Give h_i the same calibration as w_{ij} and normalize the area of h_i to 1. This new h_i becomes the new trial function w_{ij}

4) If $w_{ij} \approx$ previous w_{ij}, then the algorithm has converged, otherwise restart from step 2.

2.2.3 Level density and transmission coefficient extraction

The primary γ spectrum h_i (from previous section) is used to construct the particle vs (primary) γ coincidence matrix called first generation (FG) matrix. This is the matrix from which the NLD and γ-SF are simultaneously extracted. This matrix has a direct proportionality to the probability of decay

, and according to the Fermi's Golden Rule, the decay probability is directly proportional to the square of the transition matrix element and the nuclear level density of an E_x bin to which the nucleus is decaying. Hence, the FG matrix, $\Gamma(E_x, E_\gamma)$, can be factorized according to [10]

$$\Gamma(E_x, E_\gamma) \propto \rho(E_x - E_\gamma)\mathcal{T}(E_\gamma) \ , \tag{2.10}$$

where $\mathcal{T}(E_\gamma)$ and $\rho(E_x - E_\gamma)$ are transmission coefficient and level density at a final state $E_f = E_x - E_\gamma$. Equation 2.10 does not depend on the spin and parity of the initial and final states, which in accordance with the Brink hypothesis [18]. The experimental first generation matrix is normalized such that $\sum_{E_\gamma^{min}}^{E_x} \Gamma(E_x, E_\gamma) = 1$ for each E_x bin which is typically 200 keV wide, depending on the experimental resolution of the Si detectors. The γ transmission coefficient $\mathcal{T}$ and the nuclear level density $\rho(E_x)$ are simultaneously extracted by minimizing the χ^2 between the theoretical FG, $\Gamma_{th}(E_x, E_\gamma)$ and experimental $\Gamma(E_x, E_\gamma)$, where

$$\Gamma_{th}(E_x, E_\gamma) = \frac{\rho(E_f)T(E_\gamma)}{\sum_{E_\gamma^{min}}^{E_x} \rho(E_f)T(E_\gamma)} \ , \tag{2.11}$$

and

$$\chi^2 = \frac{1}{N_{free}} \sum_{E_x^{min}}^{E_\gamma^{max}} \sum_{E_\gamma^{min}}^{E_x} \left(\frac{\Gamma_{th}(E_x, E_\gamma) - \Gamma(E_x, E_\gamma)}{\Delta\Gamma(E_x, E_\gamma)} \right)^2 . \tag{2.12}$$

The parameter N_{free} represents the degrees of freedom and is calculated as $N = N_P - N_\rho - N_\Im$, where N_P represent the entries number in the primary γ ray matrix whereas N_ρ and $N_\Im$ are data points number in the vectors to be determined [10]. The $\Delta\Gamma(E_x, E_\gamma)$ is uncertainty in the experimental first generation. The limits E_x^{min} and E_x^{max} must be chosen such that the fitted data

originates from the quasi-continuum region, and E_γ^{min} must be selected such that low-energy γ-rays, emitted at discrete E_x and did not properly undergo first generation method, are excluded. It can be shown that once the values of $\rho(E_f)$ and $\mathcal{T}(E_\gamma)$ are obtained, equation 2.12 will have infinitely many solutions of the form

$$\bar{\rho}(E_f) = A\rho(E_f)e^{\alpha E_f} \tag{2.13}$$

and

$$\bar{\mathcal{T}}(E_f) = B\mathcal{T}(E_\gamma)e^{\alpha E_\gamma} \ . \tag{2.14}$$

The variables A, B and α are normalization parameters which are computed using neutron resonance data as explained below.

The values of A and α are acquired by normalizing $\rho(E_x)$ between the known discrete states level density and level density at the neutron separation energy, $\rho(S_n)$. The level density in the discrete states is computed by counting the number of levels which are obtained from [19], while $\rho(S_n)$ is calculated according to

$$\rho(S_n) = \frac{2\sigma^2}{D_0}\frac{1}{(I+1)e^{(-(I+1)^2/2\sigma^2)} + Ie^{(-I^2/2\sigma^2)}} \tag{2.15}$$

where the σ , D_0 and I are spin cut-off parameter at S_n, mean neutron resonance spacing and target nucleus spin in the neutron capture reactions used to obtain D_0. The D_0 and I values are extracted from [20] and σ^2 is calculated using equation 2.4. Lastly, the B parameter is computed using the average experimental radiative width, $\Gamma(S_n, I_t\pi_t)$, using [21]

$$\langle\Gamma_\gamma(S_n, I_t\pm\pi_t)\rangle = \frac{B}{4\pi\rho(S_n, I_t \pm 1/2, \pi_t)}\int_{S_n}^{0}\mathcal{T}(E_\gamma)\times\rho(S_n - E_\gamma)\sum_{J=-1}^{1} g(S_n, I_t\pm 1/2+J) \tag{2.16}$$

where $\rho(S_n - E_\gamma)$, $\mathcal{T}(E_\gamma)$, I_t and π_t are experimental nuclear level density, experimental γ transmission coefficient, spin and parity of a target nucleus in (n, γ) reactions. The spin distribution on the above equation is given by

$$g(E, I) = \frac{2I+1}{2\sigma^2} e^{-(I+1/2)^2/2\sigma^2} \ . \tag{2.17}$$

The value of $\Gamma(S_n, I_t\pi_t)$ is taken from neutron resonance data which is provided in Ref. [20]. The $\mathcal{T}(E_\gamma)$ and γ strength function, $f(E_\gamma)$ are related according to $\mathcal{T}_{XL}(E_\gamma) = 2\pi E_\gamma^{2L+1} f_{XL}(E_\gamma)$. If it assumed that statistical decays are mainly dipole then $f(E_\gamma)$ is given by

$$f(E_\gamma) = \frac{1}{2\pi E_\gamma^3} B\mathcal{T}(E_\gamma) \ . \tag{2.18}$$

2.3 Hauser-feshbach model

The Hauser-Feshbach model is a statistical formalism which allows the calculation of average (i.e. averaged over many overlapping resonances) neutron capture reaction cross sections. It assumes that the compound nucleus is excited to a continuum region where the cross section is a smooth varying function of excitation energy, which means the transmission coefficient is expected to be independent of the total angular momentum, J, of a compound nucleus. According to this model the neutron capture cross-section is given by

$$\overline{\sigma}_{jk}^{\mu\nu}(E_j^\mu) = \frac{\pi\lambda_j^2}{(2J_I^\mu + 1)(2J_j + 1)} \sum_{J,\pi} (2J+1) \frac{\mathcal{T}_j^\mu(J^\pi)\mathcal{T}_k^\nu(J^\pi)}{\mathcal{T}_{tot}(J^\pi)} \ , \tag{2.19}$$

where,

μ, ν = bound states in target I and residual nucleus respectively

$\pi\lambda_j^2$ = $0.6566/[\hat{A}_j \cdot E_j^\mu]$b

$\hat{A}_j$ = reduced mass, $A_I A_j/(A_I + A_j)$

J_I^μ = spin of μ state in the target nucleus

J_j = spin of the incident particle

$J\pi$ = spin and parity of the compound nucleus

$\mathcal{T}_j^\mu(J^\pi)$ = transmission coefficient for forming compound nucleus

$\mathcal{T}_k^\nu(J^\pi)$ = transmission coefficient at energy E_k^ν

$\mathcal{T}_{tot}(J^\pi)$ = total transmission coefficient for the decay of compound nucleus with spin and parity J^π .

The term $\mathcal{T}_k^\nu(J^\pi)$ in equation 2.19 is then calculated by

$$\mathcal{T}_k^\nu(J^\pi) = \sum_{v,X,L} \mathcal{T}_{XL}^v + \sum_{X,L} \int \mathcal{T}_{XL}(E_\gamma)\rho(E - E_\gamma, J, \pi)dE_\gamma \ . \tag{2.20}$$

where $\mathcal{T}_{XL}(E_\gamma)$ is the transmission coefficient of multi-polarity XL for a specific E_γ. The transmission coefficient of the entrance channel is calculated using the phase shifts of the scattered neutron wave, which are computed numerically from neutron optical model potentials [11].

Chapter 3

Experimental Details

The ^{186}W and ^{187}W nuclei were produced using ^{186}W(d, d') and ^{186}W(d, p) reactions in the Oslo Cyclotron Laboratory(OCL) situated at University of Oslo. This was achieved using a target thickness of 3.5 mg/cm^2 and 13 MeV deuteron beam of intensity 1.2 $\sim$ 2.1 nA. The data reduction and analysis for this experiment were based on charge-particle γ coincidence events which were detected with the CACTUS (γ detection) and SiRi (charged particle detection) arrays. The overview of OCL and details of these detector configurations are provided below.

3.1 The Oslo Cyclotron Laboratory Setup

At OCL, the cyclotron provides the pulsed light-ion beams (see figure 3.1 for illustration). The beam passes through slit $S1$ and quadrupole magnet $Q1$ where it is collimated and focused, respectively. It then proceeds to the analyzing magnet where it is bent through 90°. It then passes through slits $S2, S3$, $S4$ and quadrupole magnets, $Q2$ and $Q3$ where it is collimated to about 1 - 2 mm at the target position.

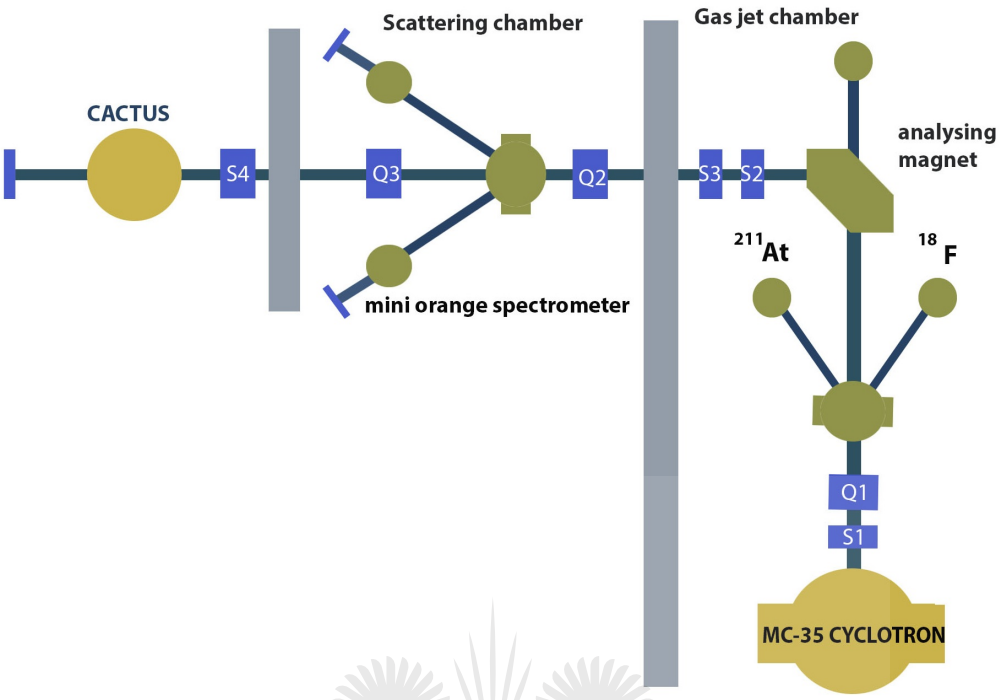

Figure 3.1: Schematic drawing of the OCL, modified from Ref. [23].

3.2 Electronics and Data Acquisition

At OCL, multichannel power supply system provides power to photomultiplier tubes of Na(Tl) detectors in CACTUS. Additionally, high voltage (HV) supplies NaI(Tl) detectors with 700 - 800V. The thick (E) and thin ΔE of SiRi array are biased each by 30V and 350V, respectively, by high precision bias units. All the signals from ΔE and E detectors are enhanced by 16-channel preamplifiers, located very close to scattering chamber to limit cable induced noise. Signals from ΔE and E array are sent to multichannel spectroscopic amplifier and timing filter amplifier (TFA) in data acquisition room. The signal from E detector triggers an event to start while signal from NaI(Tl) will trigger a stop signal in the time to digital converter (TDC) module. The time window for each event is set to $\approx$ 200 ns. The TFA sends a signal to lead-

ing edge discriminator where particle detectors signals that are in coincidence with CACTUS are taken. Once the coincidence event occurs the analog to digital converter and TDC sends information to data acquisition room [50]. The figure 3.2 shows the electronics found in data acquisition room of OCL.

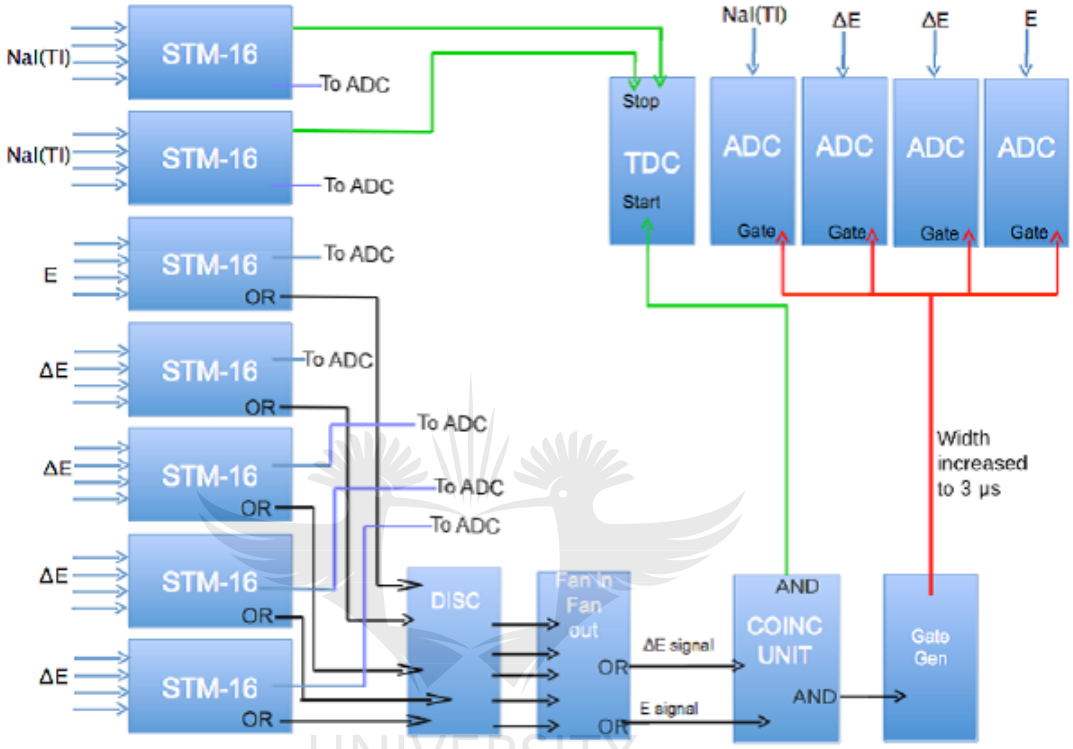

Figure 3.2: Block illustration of electronics in data acquisition room at OCL [50].

3.3 Radiation Interaction with Matter

The way radiation interacts with matter is the foundation of radiation detection and measurement. Different processes in which heavy charged particles and photons interact with matter are discussed below.

3.3.1 Charged Particles Interaction with Matter

Heavy particles, such the α particles interact with a stopping medium through i) collisional losses with the atomic electrons and ii) radiation losses (bremsstrahlung) in the vicinity atomic nuclei. The latter rarely occurs, and is considered at very low projectile energies and also depends on proton number. Upon entering the absorber, a heavy charged particle interacts simultaneously with many electrons in its path. As a result, it experiences an electric field and its energy is transfered to those atomic electrons. Depending on how close the electron is to the particle, interaction may either excite or ionize many atoms in its passage through the material. The energy loss of the particle due to each interaction with an electron is very small, but because the number of collision per length is quite large, the particle may eventually lose all its energy and stop. The path of heavy particles tend to be straight because they are not greatly deflected by collision. Once the ionization is done electrons usually to recombine with positive ions. In some detectors this recombination is suppressed to use the number of electron-ion pair as the basis of detector response. In some cases an electron may gain enough energy to cause secondary ionization. Such high-energy electrons are called δ electrons. The process of slowing down may be interpreted as average energy lost per unit path length. The rate at which charged particles lose energy per unit length is called stopping power of the absorber. The stopping power is calculated using the Bethe-Bloch formula according to [24],

$$-\frac{dE}{dx} \approx \frac{4\pi e^4 Z_p^2}{m_e v^2} N_A \rho \frac{Z_t}{M_t} \ln \frac{2m_e v^2}{I} \tag{3.1}$$

where,

Z_p = charge of incident particle

v = projectile velocity

Z_t = Absorbing material atomic number

M_t = Absorbing material atomic mass

m_e = Electron mass

e = Electron charge

ρ = Density of absorber

I = average excitation and Ionization potential .

From equation 3.1 its shown that the stopping power increases with the decreasing particle energy, except at high energies where the logarithm part of equation 3.1 dominates. It also increases with Z_p^2 and ρ. Hence heavy particles will lose a significant amount of energy in the same stopping medium.

3.3.2 γ rays Interaction with matter

Photons such as γ rays interact with matter through the following three major processes: (i) photoelectric effect, (ii) Compton scattering and (iii) pair production. In contrast to heavy particles, a γ-ray either transfers all its energy to the electron of an absorber atom and be absorbed or transfers some of its energy to be deflected through a significant angle. These types of interaction are discussed below.

Photoelectric Effect

The photoelectric effect occurs when incident photon (γ-rays) has enough energy to overcome the electron binding energy in an absorber material. The photon will transfer all of its energy to one electron of the absorber atom, leading to the emission of an electron, with kinetic energy given by

$$E_e = E_\gamma - E_b \tag{3.2}$$

where E_γ and E_b represent the energy of incoming photon and binding energy the material respectively. Since it is impossible for a free electron to absorb a photon and conserve linear momentum simultaneously, the photoelectric effect always goes for the tightly bound electrons, with an atom absorbing the recoil momentum. In photons with energies of at least 100 keV, the photoelectrons are most likely to originate from the K-shell [24]. The ejected electron leaves a vacancy, That is immediately filled by an electron from a higher energy shell or a free electron from other atoms of the absorber. As result of this process the characteristic x-rays or Auger electrons are emitted (see figure 3.3 below).

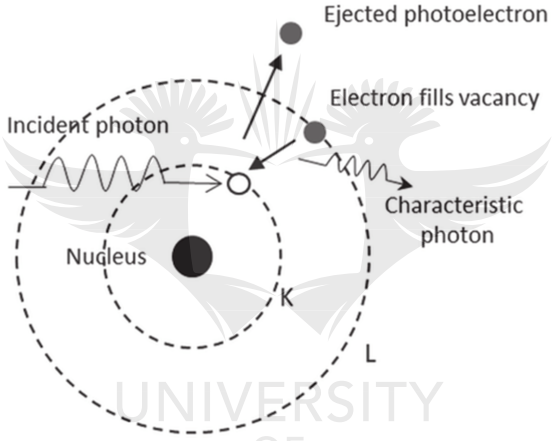

Figure 3.3: Photoelectric effect(figure modified from [25]).

In most cases they are completely absorbed very close to the primary photon-electron interaction site and their energy is kept by the stopping material. The photoelectric effect probability, for photon energies higher than 100 keV, can be approximated using [24]

$$P_{photo} \approx \frac{Z^n}{E_\gamma^{7/2}} \tag{3.3}$$

where Z is the absorber atomic number and n is the energy dependent variable which varies between 4 and 5 for 1 keV $\leq E_\gamma \leq$ 5 MeV. This equation shows a strong dependence on Z. Hence the photoelectric effect is most likely to take place in high Z materials such as lead, and is less probable for high energy γ rays.

Compton Scattering

In Compton scattering, an incident photon from a free (E_γ » E_e) is deflected by an electron at an angle θ relative to its original direction. This process is illustrated in figure 3.4. The photon transfers some of its energy, from small to a large fraction depending on the scattering angle, to the electron. The remaining scattered photon energy is calculated, based on the laws of conservation of energy and momentum, according to

$$E'_\gamma = \frac{E_\gamma}{1 + \frac{E_\gamma}{m_e c^2}(1 - cos\theta)} \tag{3.4}$$

where $m_e c^2$ is the electron rest mass.

The probability of Compton scattering per absorber atom is directly proportional to the electron number and inversely proportional to the γ ray energy.

Pair Production

Pair production is the process where by a photon of energy E $\geq$ 1022 keV is changed into an electron-positron pair in the field of an atom. The photon energy has to be greater or equal to 1022 keV so that it can be transformed

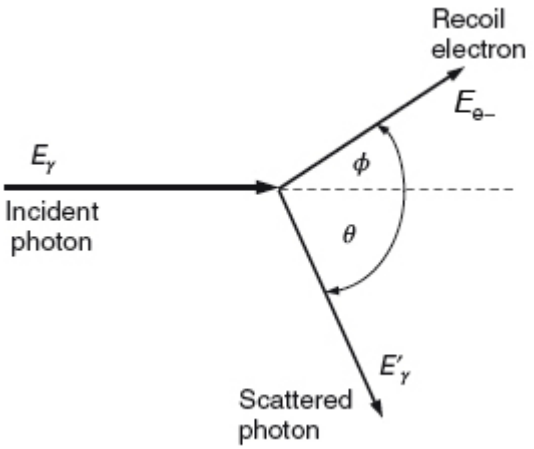

Figure 3.4: Compton effect [24].

to the individual rest masses of the positron and electron. The excess energy (E_γ - 1022 keV) of the photon is shared as kinetic energy by the positron and electron. Both these particles will be slowed by the absorber and the positron will annihilate with an electron. As a result two 511 keV photons are emitted in opposite directions in order to conserve momentum. The pair production probability increases with the increase in the absorber atomic number, Z, and incident photon energy [24]. This dependence on the Z is supported by the fact that a heavy body is required so that both energy and momentum are conserved.

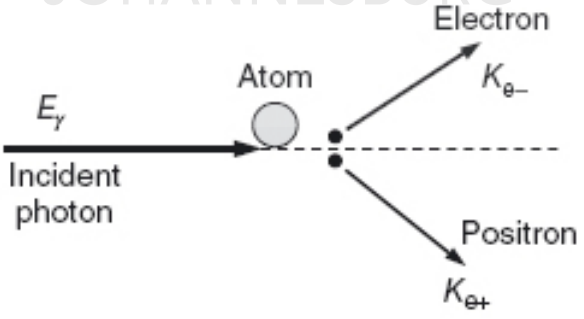

Figure 3.5: Pair Production [24].

3.4 Detectors

Currently radiation detectors are the very reliable instruments which are utilized to study nuclear reactions involving γ-rays, protons and α particles. There are many types of detectors, and each has its own advantages and disadvantages depending on the purpose of an experiment. The scintillation and semiconductor detectors which were utilized in this work are discussed below.

3.4.1 Scintillation Detectors

In scintillation detectors, incoming radiation from a reaction is absorbed in a scintillator that is located inside the detector, hence exciting its molecules and atoms. The atoms in the crystal de-excite within $\approx 10^{-8}$s by emitting visible light [24]. This light will strike the photo-cathode (photo-emissive material such as Cesium antimony) of PMT, which releases at most one electron per incident light photon. These photoelectrons are attracted to the dynodes (starting from the one closest to the photo-cathode) and multiplied. These dynodes are kept at the typical voltage of 200 - 400 V and made of secondary emissive materials such as magnesium oxide (MgO), beryllium oxide(BeO) and gallium phosphide(GaP) coated on stainless steel substrate electrode. Hence the incident photo-electrons eject secondary electrons from the first dynode. In this way the number of electrons is multiplied. The multiplication will depend on the potential difference of the dynode and energy of electrons that are striking it. The electrons emerging from a dynode are attracted to the next dynode which has 50 - 150 V higher potential difference than the preceding one. The multiplication of electrons continues up to the last dynode as illustrated in figure 3.6. This process takes place through typically 9 to 12 dynodes in total, until a large number (typically 6^{10} for 10-stage photomultiplier tube with average multiplication factor of 6 per dynode) of electrons is produced and collected in the anode. A good scintillator detector must be

transparent to its own light and have high chances of converting the absorbed energy into fluorescent light. In most scintillators the light output is directly proportional to the absorbed energy, which makes them the right candidates for energy measurements despite poor linearity and resolution. Other advantages of scintillators are fast response, recovery times and variety of sizes. A reflective foil is always needed for recapturing the escaping light. Scintillators have two categories namely organic and inorganic scintillators. For this work the inorganic NaI(Tl) crystal, was used.

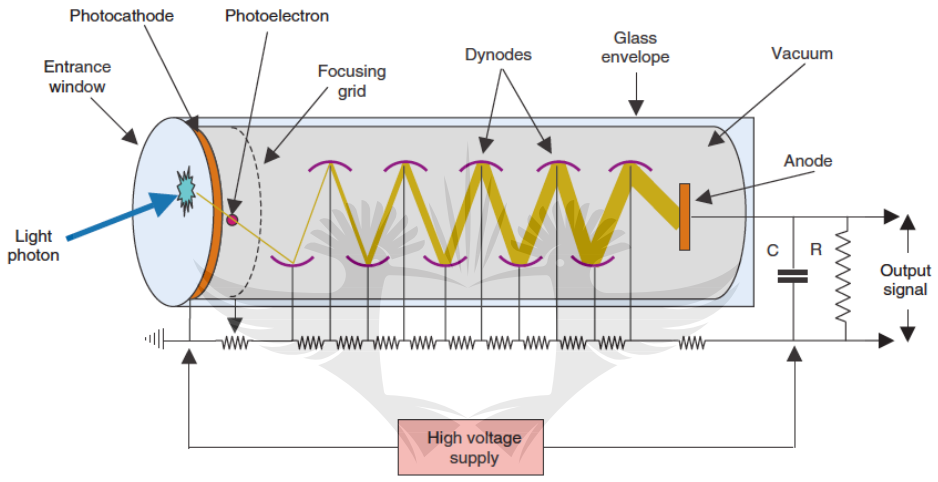

Figure 3.6: Schematic of scintillation detectors [24]

3.4.2 Semiconductor Detectors

Semiconductor detectors are based on the creation of the p-n junction. This is a region at the boundary between an n-type (such as silicon doped with phosphorus) and p-type (such as silicon doped with boron) semiconductor materials [24]. The n-type material electrons move across the boundary into the holes of the p-type material, and thus creating a depletion region. This depletion zone represents the active volume of the detectors and is significantly enlarged by applying an external reverse bias voltage to the junction. The electron-hole pairs are created when an incident radiation transfers the energy

on depletion zone. The newly framed pairs are swept out by electric field such that electrons are collected at the anode and holes in the cathode (see figure 3.7 for illustration). Thus a voltage signal that can be translated to the energy deposited is produced. Semiconductors such as silicon detectors require a typical energy of 3.8 eV to create an electron-hole pair. This is lower by at least ten times in when comparing to other types of detectors such as scintillation detector. Thus, for the same amount of energy deposited, semiconductors will produce a considerable large number of charge carriers than any other type of detector. Hence, their energy resolution is greatly improved. Furthermore, signal pulse height of these detectors is proportional to the incident radiation energy and therefore their response is very linear. The semiconductor detectors used in this study are silicon detectors which are very useful for detection of charged particles. They have approximately 100% intrinsic efficiency because most of the incident charged particles will be able to ionize the depletion region. This is because the experimental setups are usually chosen such that the depth of the depletion region is deeper than the incident particle's range. On the other hand semiconductor detectors can experience thermal generation of electron-hole pairs. This gives rise to the leakage current that leads to degradation in the signal to noise ratio of the output pulse. However, this is usually only significant in germanium detectors which have small bandgap and not silicon detectors.

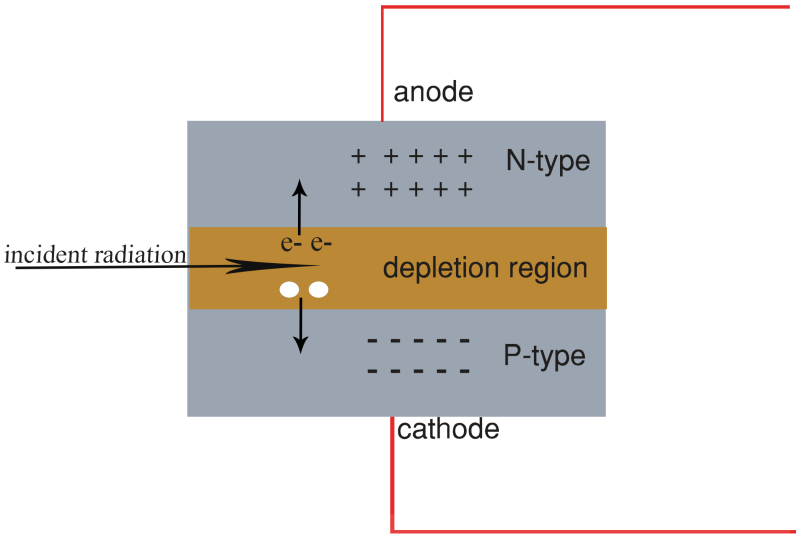

Figure 3.7: Schematic layout of semiconductor detectors.

3.5 CACTUS Multi-detector Array

the CACTUS multi-detector array used to measure energies γ rays. It consists of 26 NaI(Tl) detectors (5" $\times$ 5" crystals) which are placed at a radius of 22 cm from the target and mounted on a spherical frame, resembling a cactus plant (see figure 3.8) and hence its name. Conical lead collimators of 10 cm thickness and 7 cm diameter are placed at the front surface of these detectors, giving a solid angle of 17 % of 4π sr. The cross-talk between adjacent detectors is eliminated by 3 mm thick lead sheets surrounding each NaI(Tl) detector. Furthermore a copper absorber with thickness 2 mm is also placed in front of each detector to suppress x rays. In total this array has an efficiency and energy resolution of $\approx$ 14.1 % and $\approx$ 7 % FWHM for 1.3 MeV γ-ray transitions.

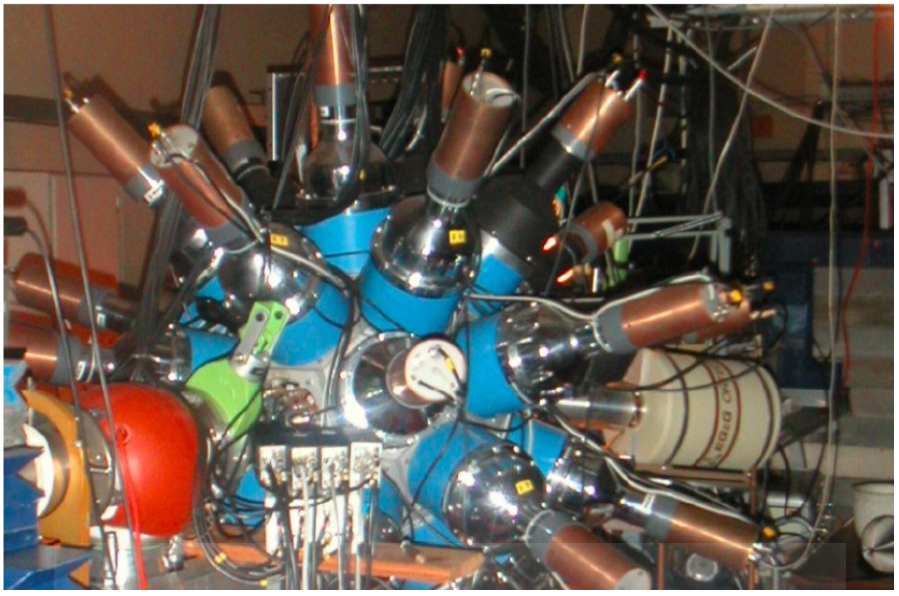

Figure 3.8: The CACTUS array at OCL [23].

3.6 The SiRi Array

The SiRi (silicon ring) array comprises 8 (with trapezoid shape) $\Delta E - E$ telescope detectors forming a ring (see figure 3.9). The ΔE and E detectors are made with $\approx$ 130 μm and 1550 μm thick Silicone detectors, respectively [26]. The front thinner detectors are separated by few mm from the thicker ones. This makes it possible to separate various charged ejectiles such as protons, deuterons, ^{3}He and α, due to their different masses and energy loss through the ΔE detectors. The position of this detector telescope relative to the target and beam axis is illustrated in figure 3.10.

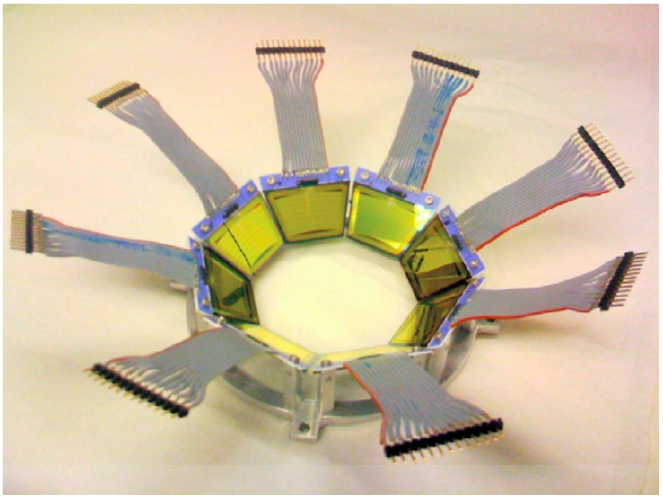

Figure 3.9: The SiRi particle telescope [26].

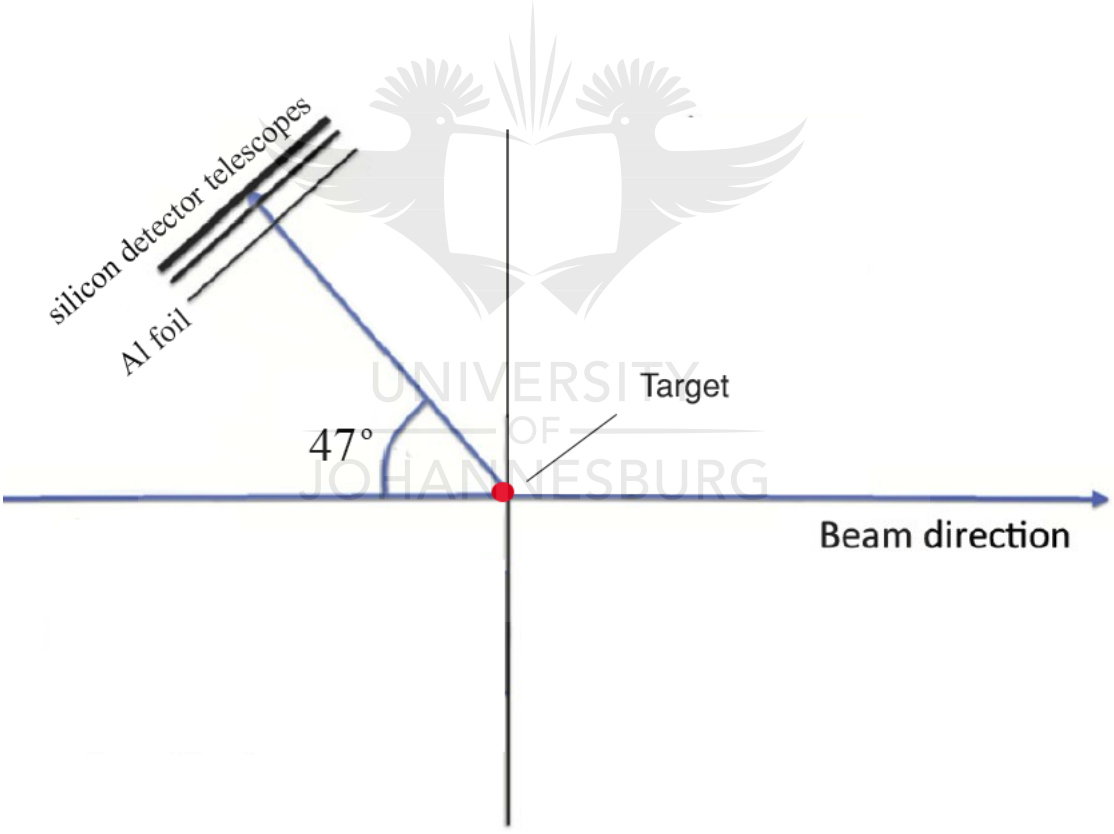

Figure 3.10: The placement of Si particle-telescope with respect to beam direction [26].

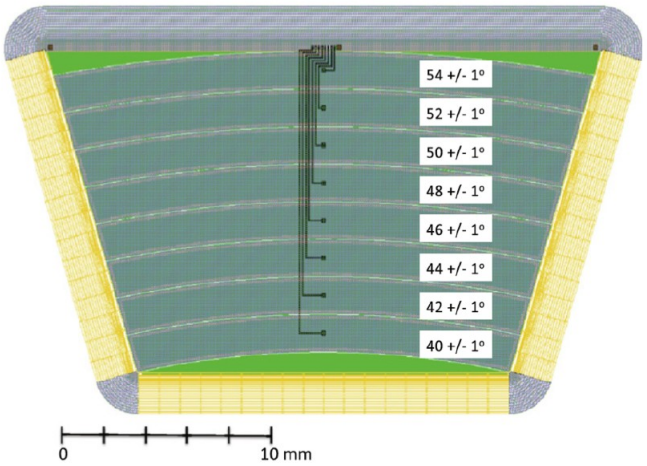

Figure 3.11: Layout of one ΔE detector [26].

Each ΔE detector is divided 8 times (see figure 3.11), while E is not(making 8 ΔE strips per E), miking a total of 64 $\Delta E - E$ sub-telescopes. This segmentation is used to reject pile-up events in each E detector shared by 8 ΔE strips, by ensuring that signal comes from one ΔE pad per time. The mean scattering angular range covered by each detector telescope is 40° to 54° in steps of 2° per strip. In front of the segmented ΔE modules, an aluminum foil cone with 10.5 μm thickness is placed to shield the SiRi array from δ electrons ejected from the target atoms during the experiment. This setup covers a total solid angle of 6 % of 4π sr and gives a typical energy resolution of 200 keV for d elastic peak.

Chapter 4

Analysis and Results

4.1 Silicon Detectors Calibration

The silicon detectors were calibrated by fitting the experimentally observed $\Delta E - E$ matrices to the theoretically calculated ones. One of the theoretical $\Delta E - E$ matrices are shown in figure 4.1 and they were calculated using the Bethe-Bloch formula (see equation 3.1). The horizontal and vertical axes are energies expected to be deposited by charged particles in ΔE and E detectors, respectively. This calculation also accounts for energy losses in the Al foil used to shield silicon detectors from δ-electrons.

The corresponding calibrated ΔE-E plot is shown in figure 4.2 (a). It clearly reveals all three $banana - like$ energy distributions which correspond to the ^{186}W(d, p),^{186}W(d, d) and ^{186}W(d, t) reaction channels. The same calibration was also done for the ^{12}C(d,p) and ^{12}C(d,d) experimental data, which was needed for the calibration of NaI(Tl). It is also shown in figure 4.2 (b).

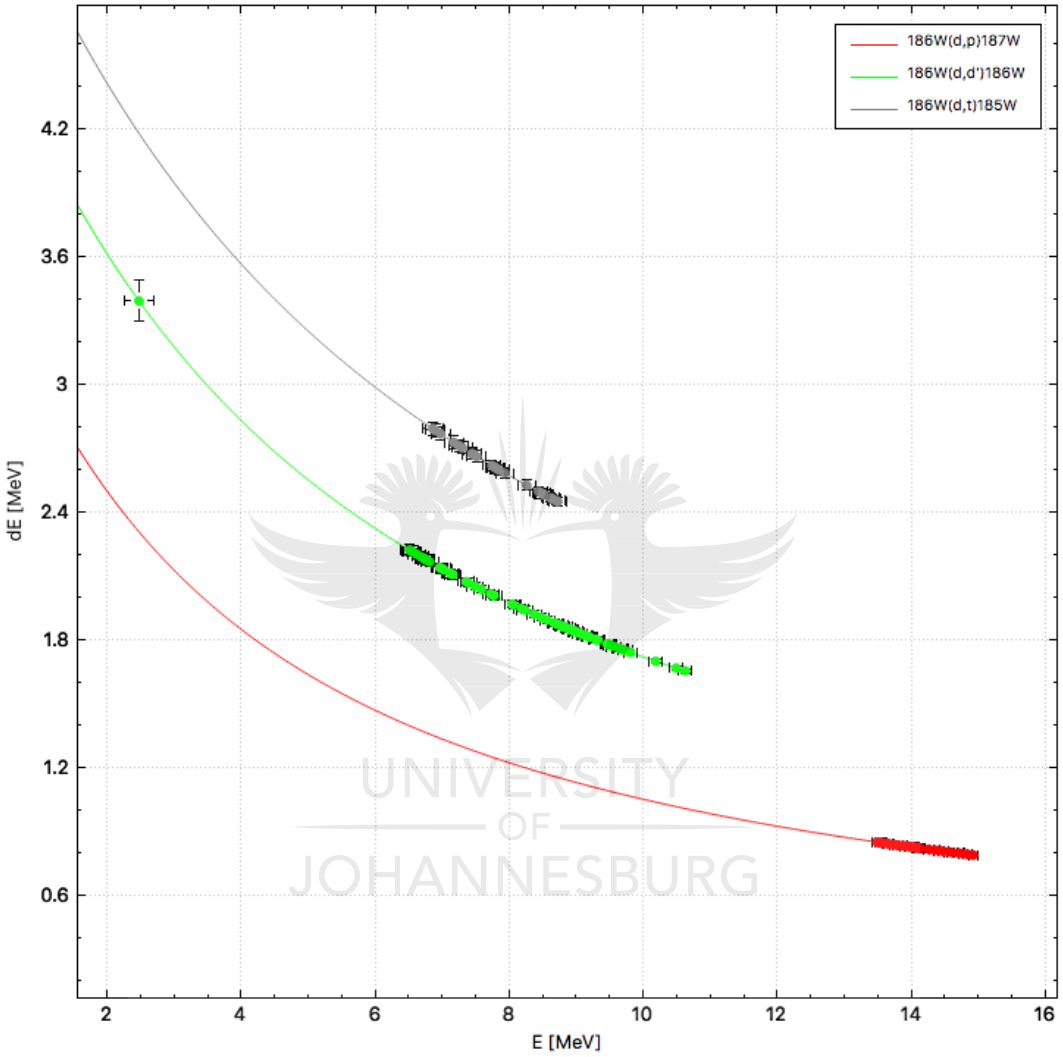

Figure 4.1: The simulated $\Delta E - E$ plot of the first ring. Data points shows calculated states necessary for calibration.

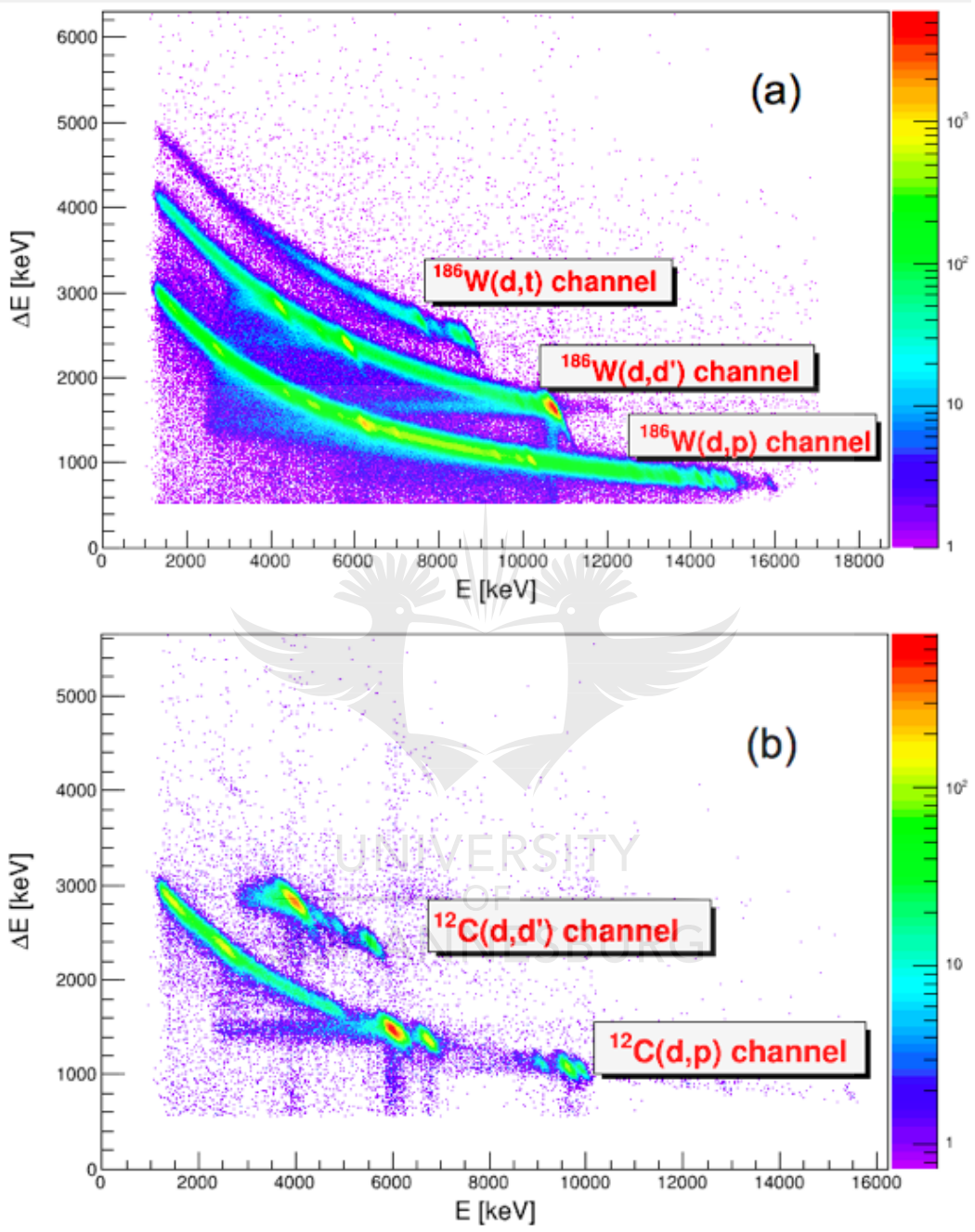

Figure 4.2: The calibrated $\Delta E - E$ plot for $^{186}W(d, X)$ (a) and $^{12}C(d, X)$ (b) reactions.

4.2 Calibration of NaI detectors

The linear calibration of NaI(Tl) detectors was achieved by using the 764 and 3089 keV γ rays of ^{13}C which was produced in ^{12}C(d,p) reaction. A 2D gate was set on the proton channel of figure 4.2 (b). The energies of these selected charged particles where converted into the excitation energy of ^{13}C nucleus, using the kinematics and Q-value of the reaction. The resultant excitation energy spectrum of ^{13}C is shown in figure 4.3. The γ ray spectra used for calibration were obtained by gating on 3089.4 and 3853.8 keV excitation energy peaks. One of these spectra is shown in figure 4.4.There are 26 spectra of this nature which were use to calibrate all 26 NaI(Tl) detectors of the CACTUS array with the resolution of $\approx$ 14.1 %.

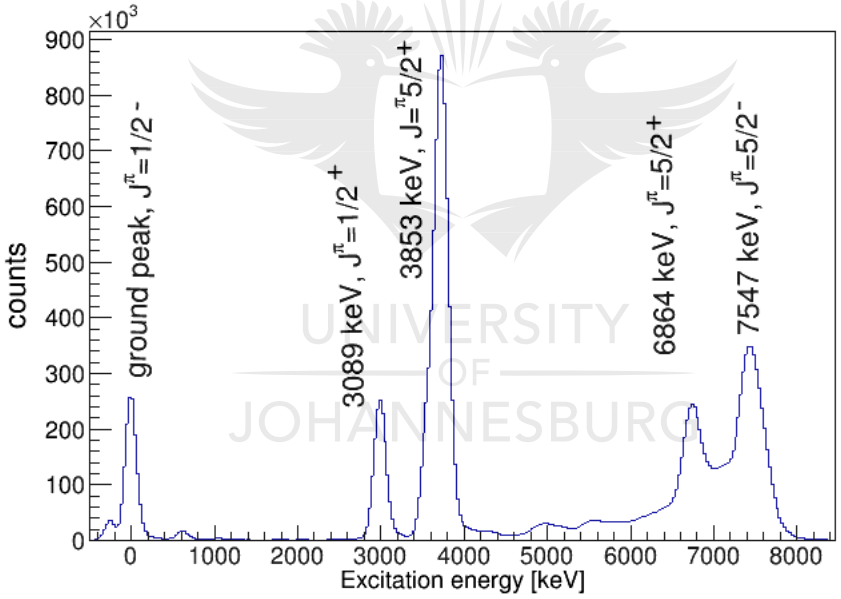

Figure 4.3: The excitation energy spectrum for ^{13}C obtained from p energies out γ ray coincidence requirements. These are calculated from energies measured on the SiRi array with resolution of 200 keV for d elastic peak

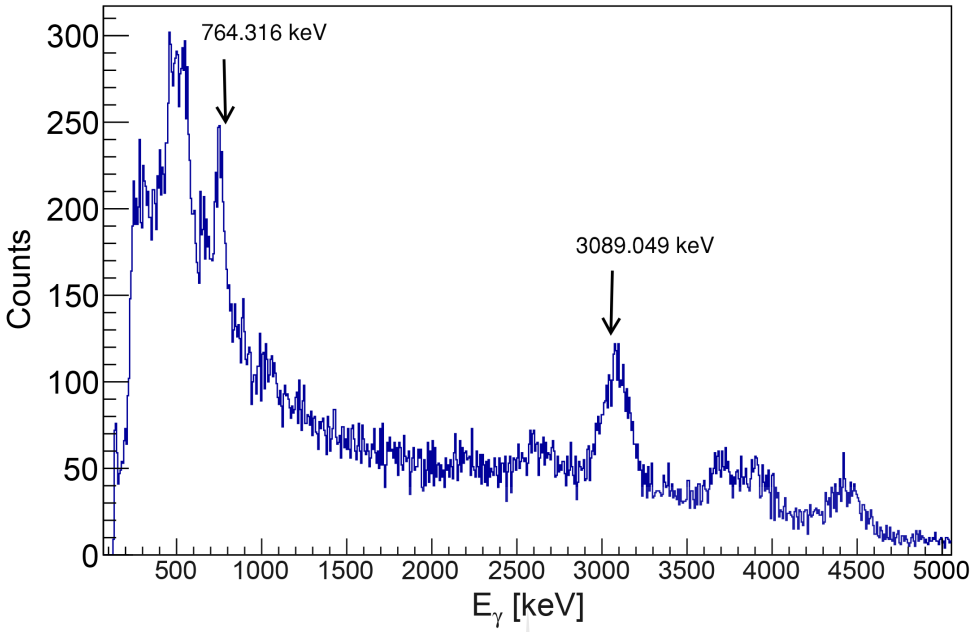

Figure 4.4: The γ spectrum of ^{13}C used for calibration.

4.3 Time Calibration

During the experiment, silicon and NaI(Tl) detector's signals are used as start and stop signals of the Time-to-Digital Converter (TDC), respectively. The rise time which is the time it takes for a signal to reach a voltage specific level, depends on its amplitude. The low energy events have longer rise time compared to high energy events. Hence the low energy signals will cross the discriminator threshold later in time compared to the higher energy ones. This effect is known as $walk - effect$ and is demonstrated in the time vs γ-energy matrix shown in figure 4.5. It is corrected by fitting a function of the form

$$t(x) = a + \frac{b}{x + c} + dx + 200, \tag{4.1}$$

to the energy vs time matrix and find values for coefficients a, b, c and d for the energy vs time matrix. Where $t(x)$ and x are channels corresponding to

time and γ ray energy, respectively. The intercept, 200, of equation 4.1 is for ensuring that all prompt time peaks are aligned and positioned at channel 200, as shown in the figure 4.6. Similar matrices were obtained for the $^{186}W(d, d')$ reaction channel.

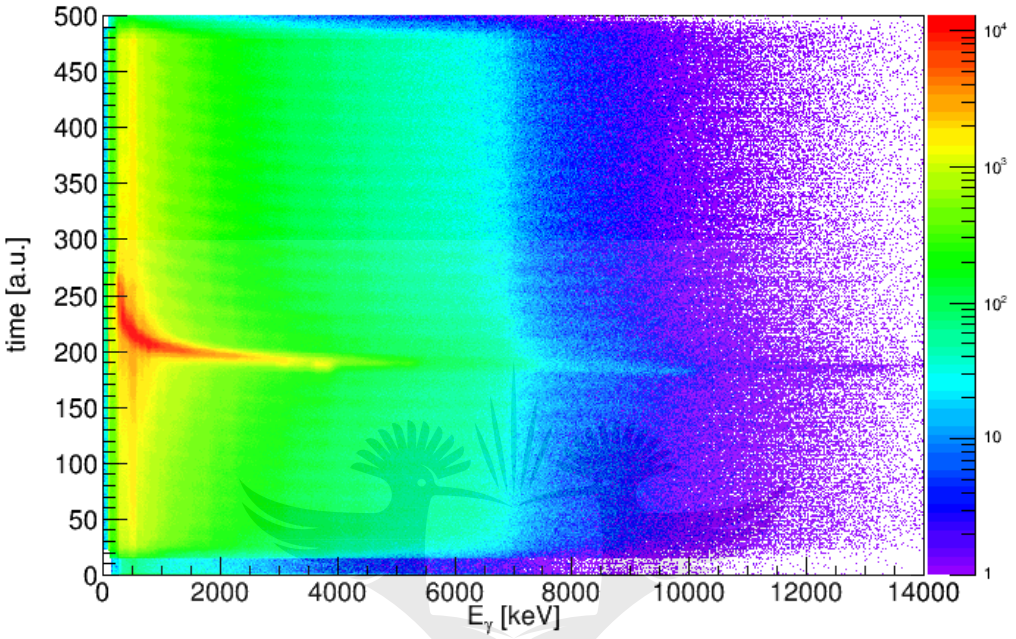

Figure 4.5: The uncorrected energy vs time matrix of the CACTUS multi-detector array for the ^{186}W(d, p) reaction.

The time spectra of ^{186,187}W nuclei were obtained by projecting their corresponding energy vs time matrices onto the time-axis. These are provided in the figures 4.9 and 4.10 and used in the next section for extraction of particle-γ coincidence events.

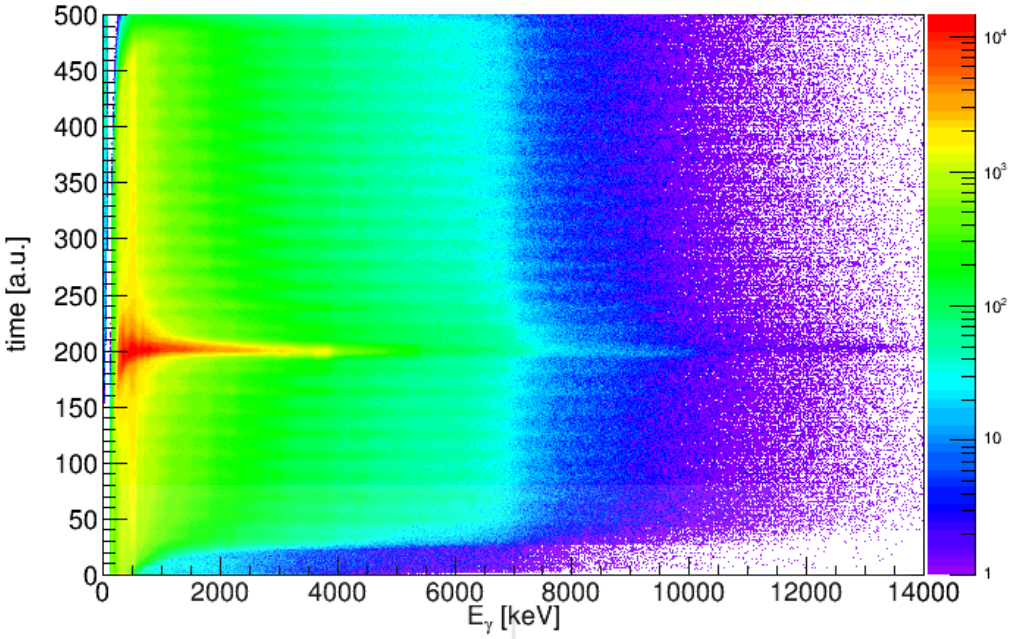

Figure 4.6: The γ energy vs time matrix of ^{186}W(d, p) corrected for *walk* effect.

4.4 Particle γ Coincidence Matrices

The Oslo Method, utilized for extraction of NLD and γ-SF, is based on particle γ coincidence events. These were extracted for both ^{186}W and ^{187}W nuclei, by gating on the proton and deuteron particles (see figures 4.7 and 4.8) and the corresponding prompt time peaks.

The prompt time peaks (see figures 4.9 and 4.10) were both $t2 - t1 = 70\ ns$ wide. The excitation energy, E_x, vs γ energy matrices which were generated from these coincidence events are provided in figures 4.11 (a) and (b). They were also corrected for random events by subtracting events were that obtained by gating on the corresponding random time peaks (see figures 4.9 and 4.10) which are also $t'2$-$t'1 = 70$ ns wide . These excitation energies were constructed from p and d energies using kinematics and Q_{value} of reactions.

The diagonal line ($E_x = E_\gamma$ lines) in the E_x vs E_γ matrices represent direct

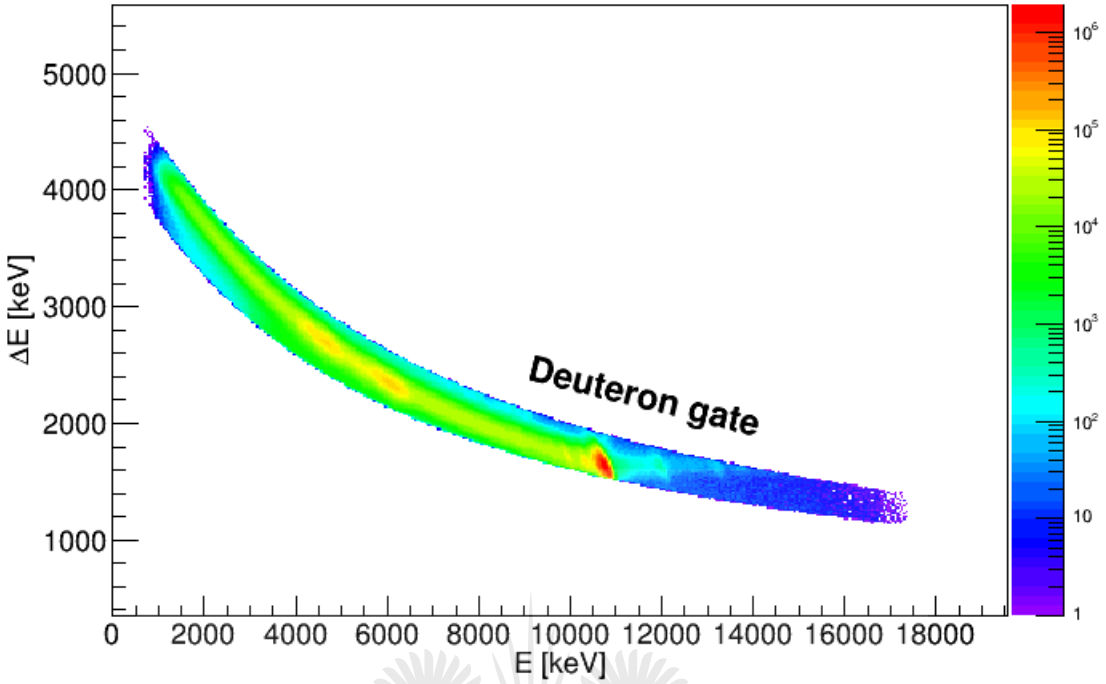

Figure 4.7: The $\Delta E - E$ plot for the ^{186}W$(d, d')^{186}$ gate.

decays to the ground states and also show that every excited state, indeed, emitted γ rays with energies less than or equal to the excitation energy. Thus, the observation of this diagonal line also confirms that both NaI(Tl) and Si detectors were properly calibrated. There is also a decrease in the number of counts at $E_x \approx S_n$, in the case of ^{186}W, because above this energy the ^{186}W$(d,$ $p\ n\ \gamma)$ starts competing with ^{186}W$(d,$ p$\gamma)$ channel. This effect is not visible in the ^{186}W matrix because the chosen reaction could not excite this nucleus up to S_n. However, this was constructed using the same gain coefficients and kind of kinematics used in the case of ^{187}W, and thus providing confidence in the E_x vs E_γ matrix of ^{186}W.

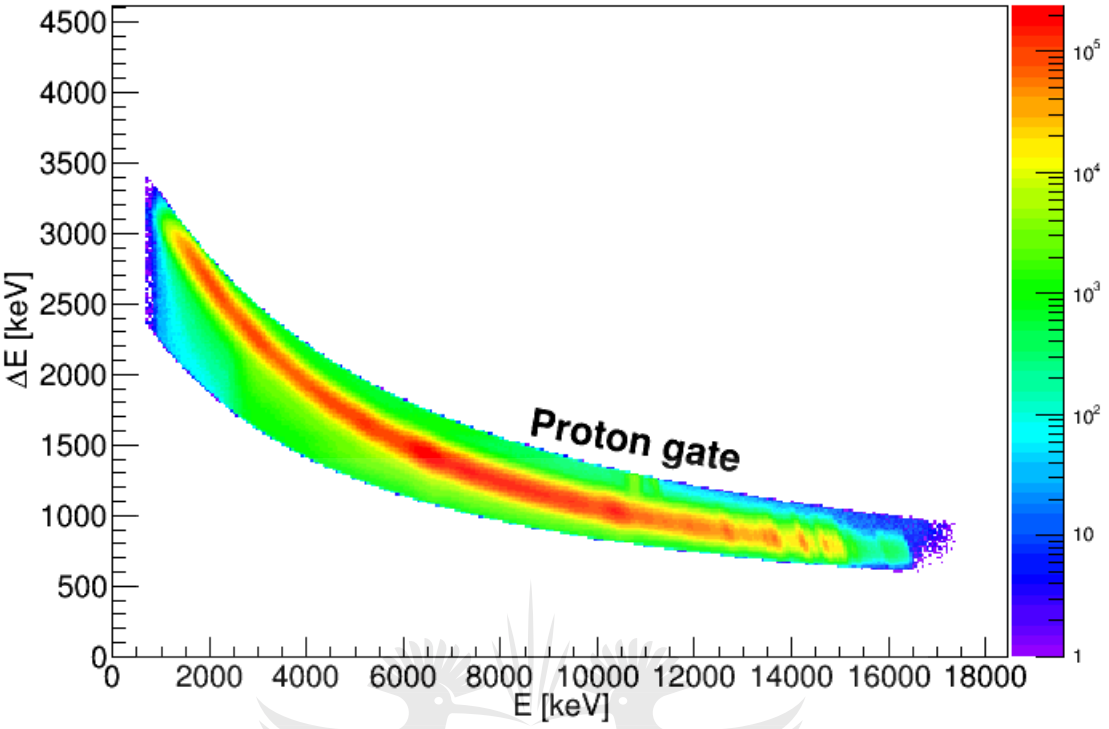

Figure 4.8: The $\Delta E - E$ plot for the $^{186}\mathrm{W}(d, p)^{187}$ gate.

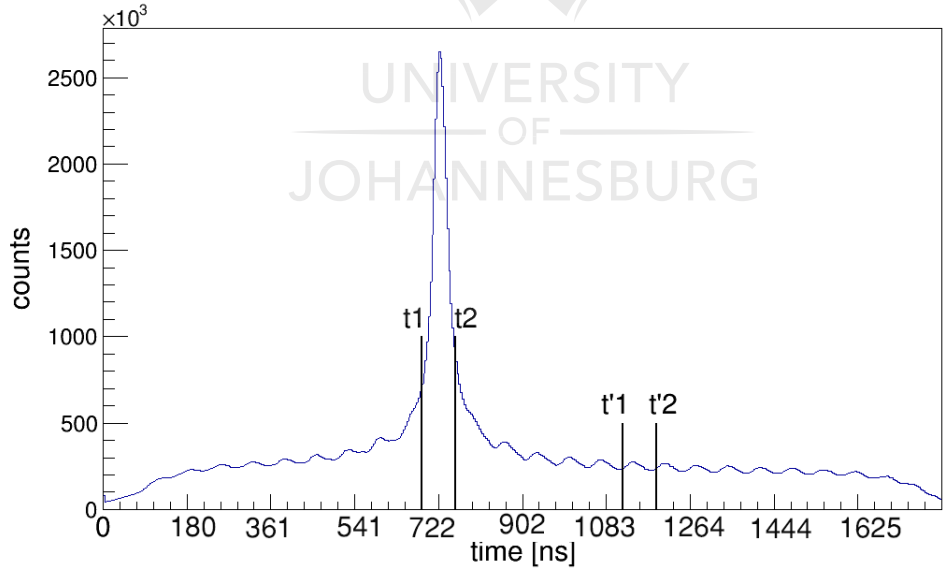

Figure 4.9: The time-axis projection of γ energy vs time matrix for $^{187}\mathrm{W}$ (figure 4.6) after time calibration and walk correction. $t1$ and $t2$ are used to gate on prompt peak while $t'1$ and $t'2$ gate on random events.

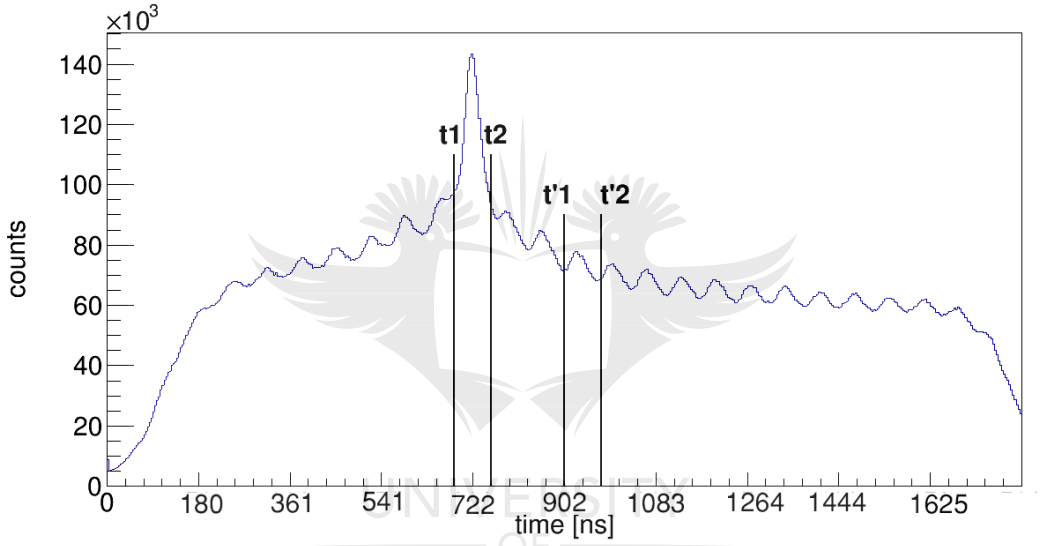

Figure 4.10: Time axis projection of time vs γ energy matrix for ^{186}W.

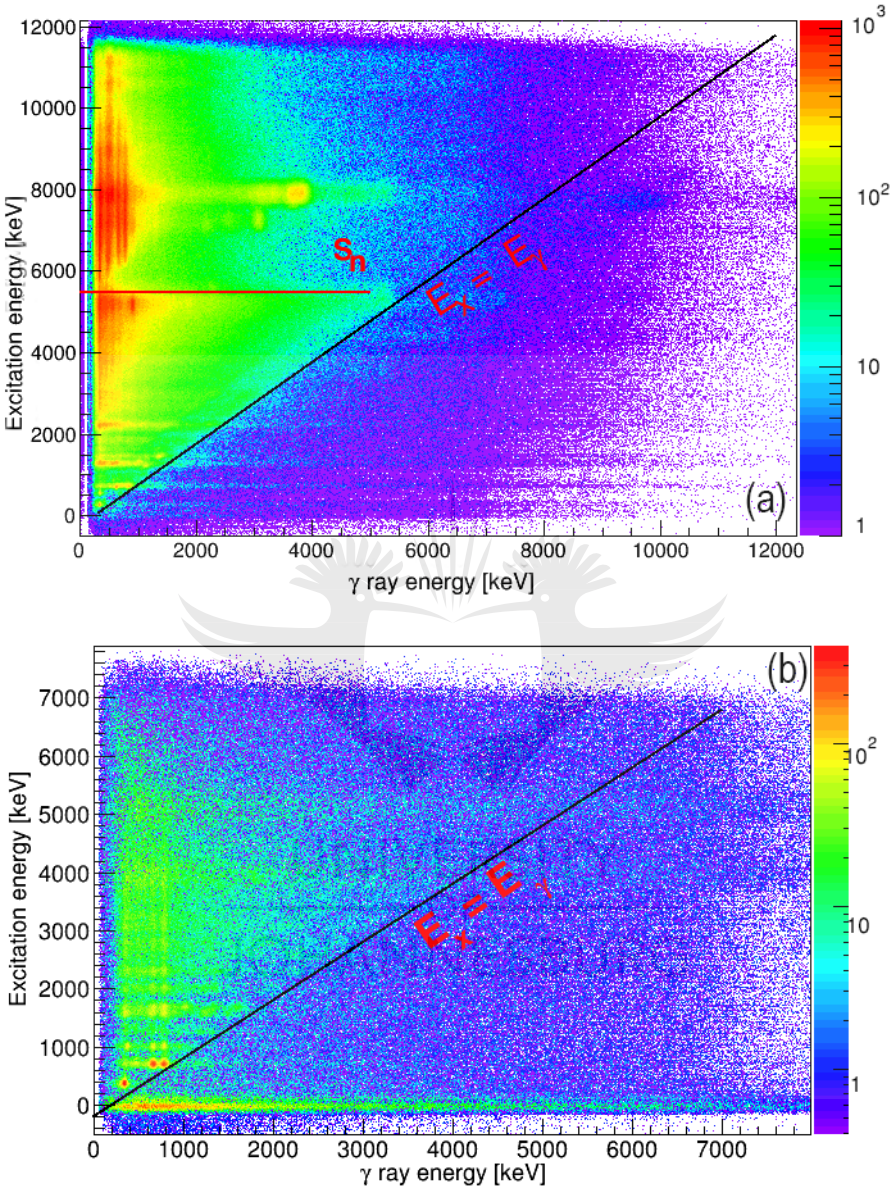

Figure 4.11: The particle-γ coincidence matrix of (a) $^{186}\mathrm{W}(d,p)$ and (b) $^{186}\mathrm{W}(d,d')$.

4.5 Nuclear Level Densities and γ Strength Functions

The continuum γ ray spectra contained in the E_x vs E_γ matrices, which are provided in figures 4.11 (a) and (b), still contain contributions from Compton scattering, pair production, and single and double escape peaks. To extract the γ-SF and NLD with the Oslo Method, we need primary-γ spectra (also know as first generation γ spectra) that have only full-energy peaks. Thus, the continuum gamma spectra are unfolded using the iterative method which is discussed in Section 2.2.1 . These unfolded spectra are then used to extract primary γ ray spectra with the first generation method which is also discussed in Section 2.2.2. The primary γ ray matrices, also known as first generation matrices, for both W isotopes are shown in figure 4.12 and 4.13. Both matrices show holes of little to no data. This is an artificial effect which is due to the over subtraction of counts in the first generation iteration method. When selecting an area of extraction for the statistical properties, areas with over subtraction are avoided to reduce any further uncertainties.

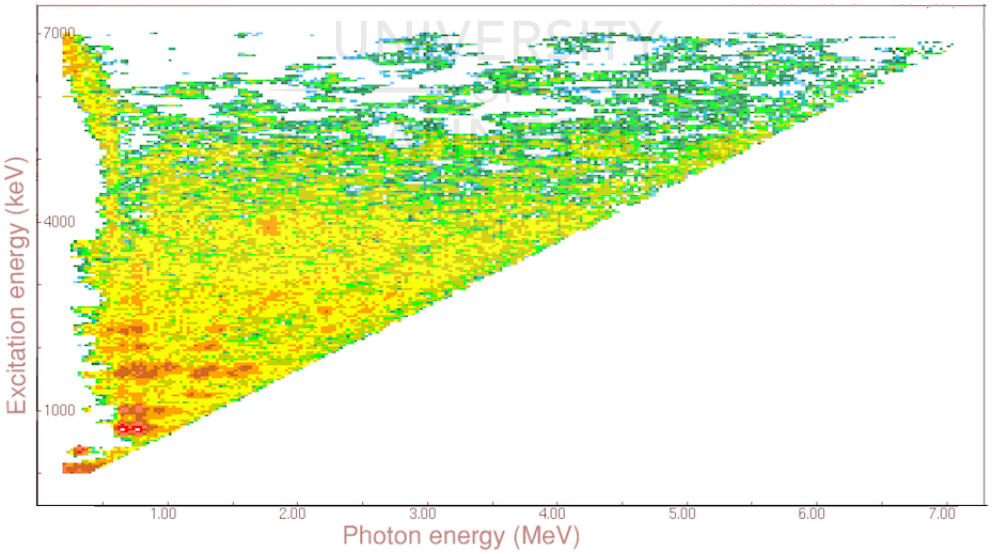

Figure 4.12: First generation matrix for ^{186}W nucleus.

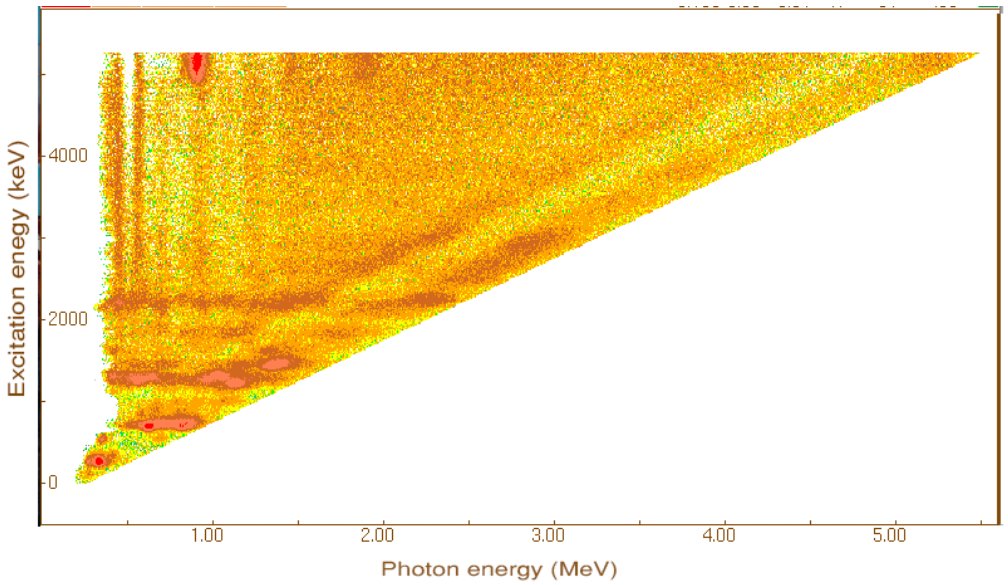

Figure 4.13: First generation matrix for ^{187}W nucleus.

It is these matrices from which the NLD and γ-SF are extracted. To achieve this, we define a theoretical first generation (FG) matrices according equation 2.11 and fit them to both experimental FG matrices using χ^2 minimization as defined in equation 2.12. This fit is performed in each, 200 keV wide, excitation energy bin in the quasi-continuum regions. During this χ^2 minimization the nuclear level density and γ transmission coefficient are treated as free parameters. Hence, they are simultaneously extracted, for each nucleus, when the χ^2 has converged. It is difficult to tell with certainty the excitation energy where the quasi-continuum region begins. Hence the lowest energy above which FG matrices are fitted were chosen such that these fitted regions comprise continuous distribution of counts and no obvious discrete energy peaks. Furthermore, the unfolding method fails at γ ray energies below 1 MeV. These are also excluded in the extraction of the statistical nuclear properties. The fitted E_x vs E_γ regions are $E_\gamma > 1$ MeV and 2.5 MeV $< E_x <$ 5.7 MeV for ^{186}W, and $E_\gamma > 1$ MeV and 2.3 MeV $< E_x$ 5.2 MeV for ^{187}W. The goodness of fits are also illustrated in figure 4.14 and 4.15 and they show that the experimental and theoretical FG matrices agree reasonable well within error bars.

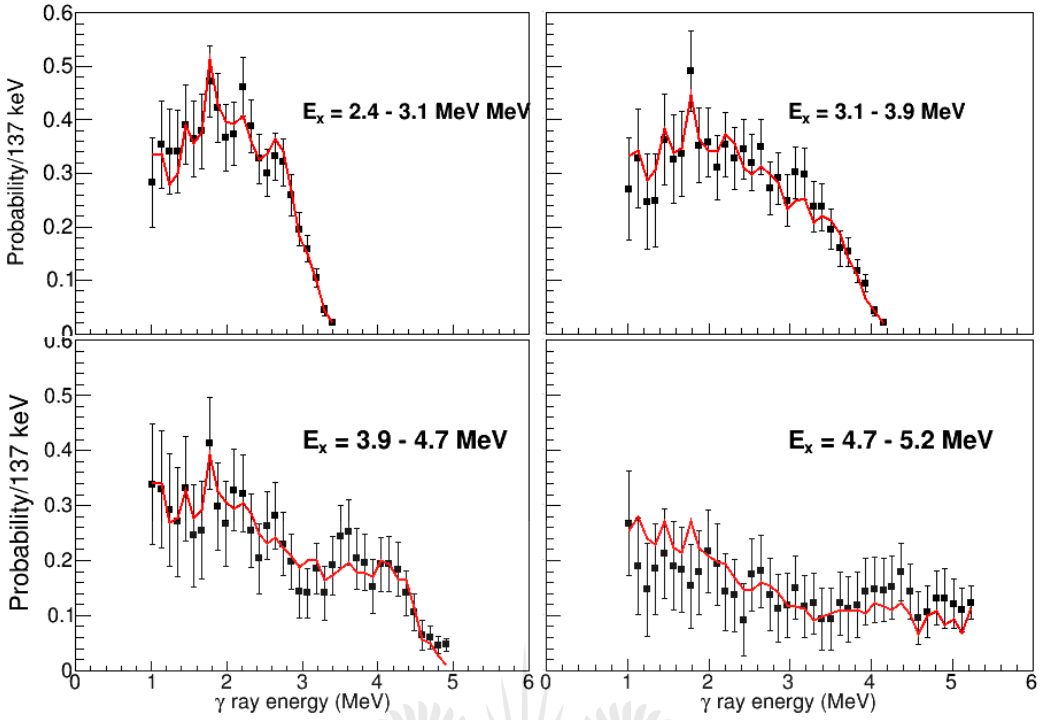

Figure 4.14: The goodness of fit for the first generation matrix of ^{186}W. The y-axis represents γ decay probability of particles at specific excitation energy

The resultant transmission coefficients , $\mathcal{T}(E_\gamma)$, and nuclear level densities, $\rho(E_x)$, obtained at this stage are just mathematical solutions possible after the χ^2 minimization, and not necessarily the actually transmission coefficients and nuclear level densities of ^{186,187}W nuclei. However, it has been shown that infinitely many of such solutions can be found and written in the functional form shown in equations 2.13 and 2.14. These were normalized to the known level density of discrete states and the level density at separation energy, $\rho(S_n)$, calculated at the neutron separation energy. In this work the discrete states were taken from [19], while the $\rho(S_n)$ was calculated using equation 2.15 which is is directly proportional to the Back-Shifted-Fermi-Gas spin cut-off parameter and inversely proportional to the average neutron resonance spacing.

The normalization parameters for both nuclei are shown in Table 4.1. The neutron resonance spacing, D_0, and Γ_γ for ^{187}W were obtained from Ref. [20],

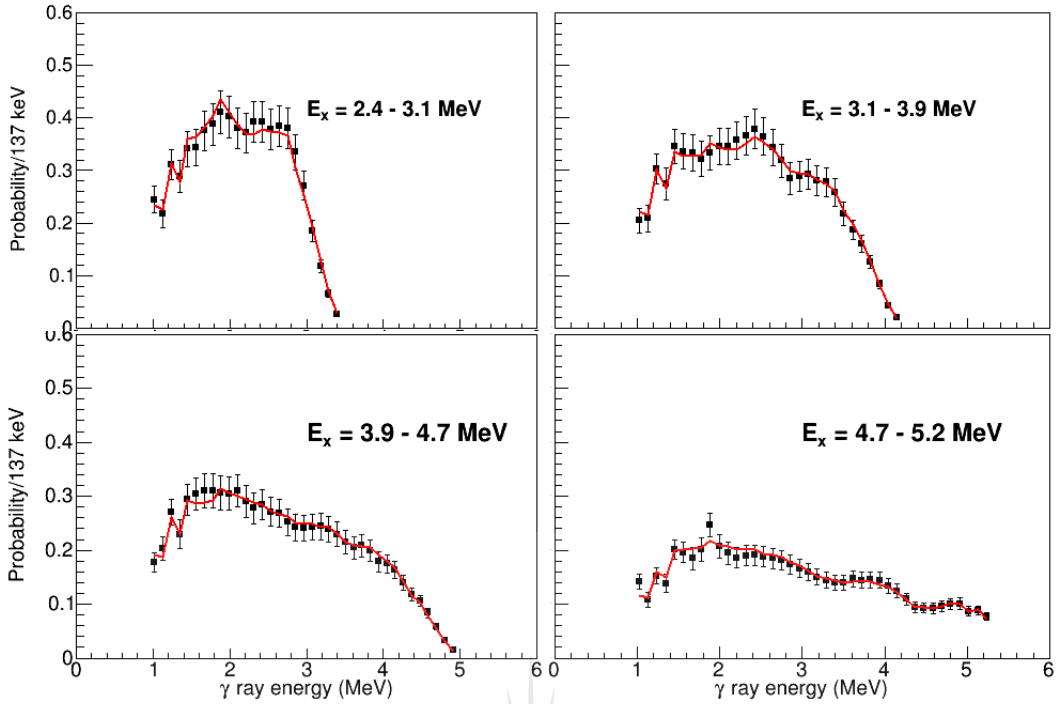

Figure 4.15: The goodness of fit for the first generation matrix of ^{187}W.

Isotope	σ	D_0 (eV)	$\rho(S_n)$ (10^5MeV^{-1})	Γ_γ (meV)	T (MeV)	E_0 (MeV)
^{186}W	4.87	7 ± 0.7	43.37 ± 9.192	74 ± 14.8	0.546	-0.826
^{187}W	4.75	99 ± 8.0	10.66 ± 1.70	51 ± 7.0	0.535	-1.625

Table 4.1: The normalization parameters of W isotopes

while for ^{186}W they are unavailable in the literature since ^{185}W is unstable. Thus the neutron resonance spacing was obtained by normalizing the $\rho(E_x)$ such that it has the same slope as ^{187}W nuclear level density as shown in figure 4.16

The corresponding Γ_γ was estimated using a TALYS reaction code's spline fit. This normalization approach has recently been applied in [29] for Lanthanum isotopes. This is because it is expected that the nuclear level density of the neighboring isotopes has the same slope as it has been observed in other nuclear species [30; 31; 32]. The normalized nuclear level densities of ^{186,187}W nuclei are shown in figures 4.17 (a) and (b). The dotted lines are the interpolation,

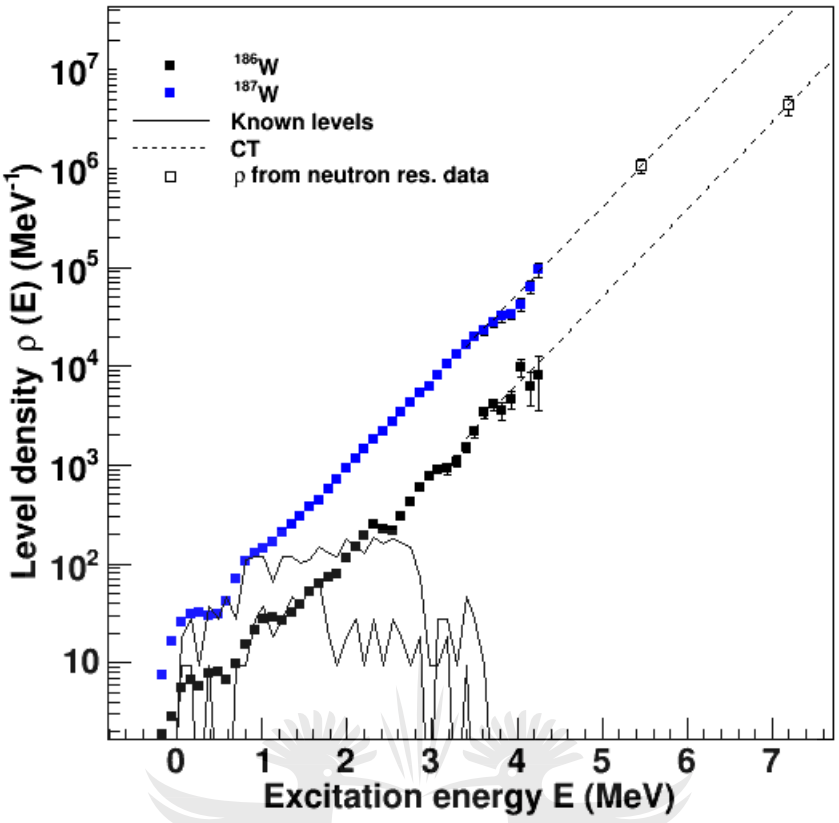

Figure 4.16: The nuclear level density slope comparison for D_0 estimation of ^{185}W.

obtained using the CT Model, between the experimental nuclear level density and $\rho(S_n)$. This normalization yields values for the A and α parameters of equations 2.13 and 2.14. The value of the normalization parameter B of equation 2.14 is computed with equation 2.16 which is based on the experimental and estimated average radiative width, Γ_γ and average neutron spacing D_0. This normalized $\mathcal{T}(E_\gamma)$ is converted into the γ strength functions, $f(E_\gamma)$, according to equation 2.18. The resultant values for $f(E_\gamma)$ of ^{186,187}W are shown in figures 4.18 (a) and (b).

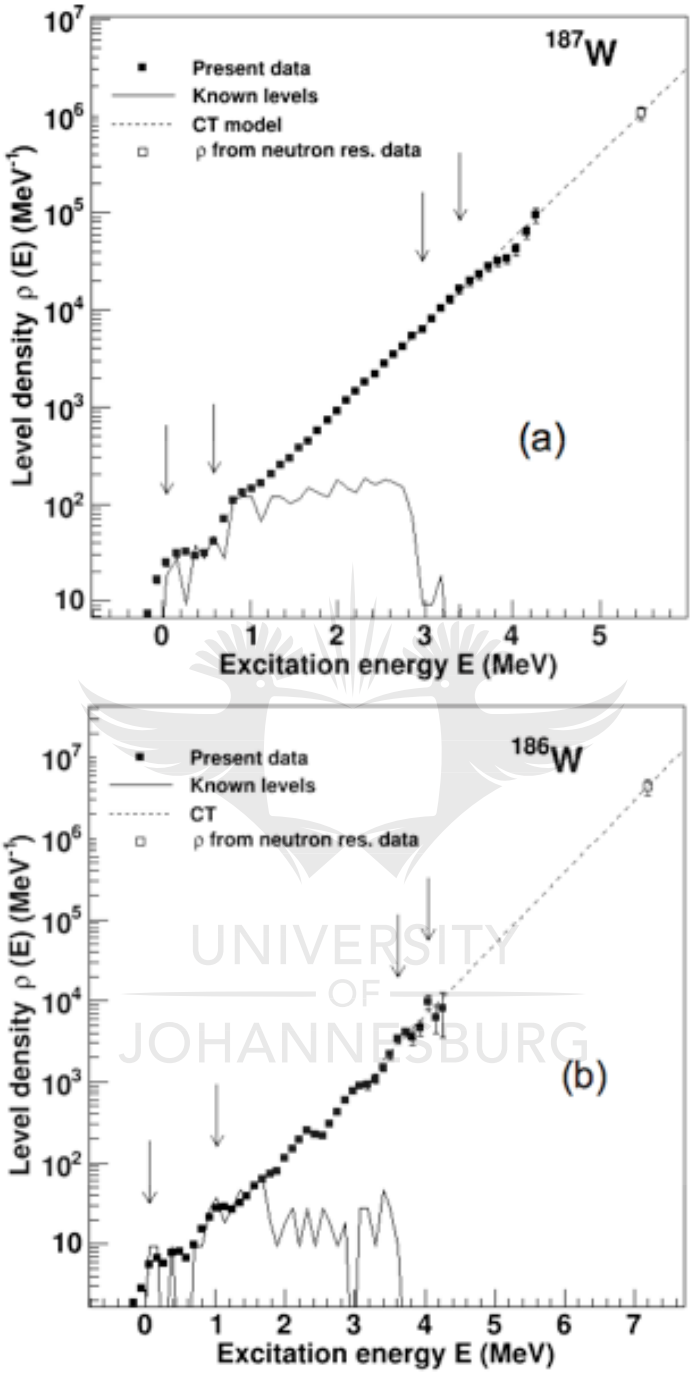

Figure 4.17: Nuclear Level Density for ^{187}W (a) and ^{186}W (b). The arrows are just for selecting the region for normalization

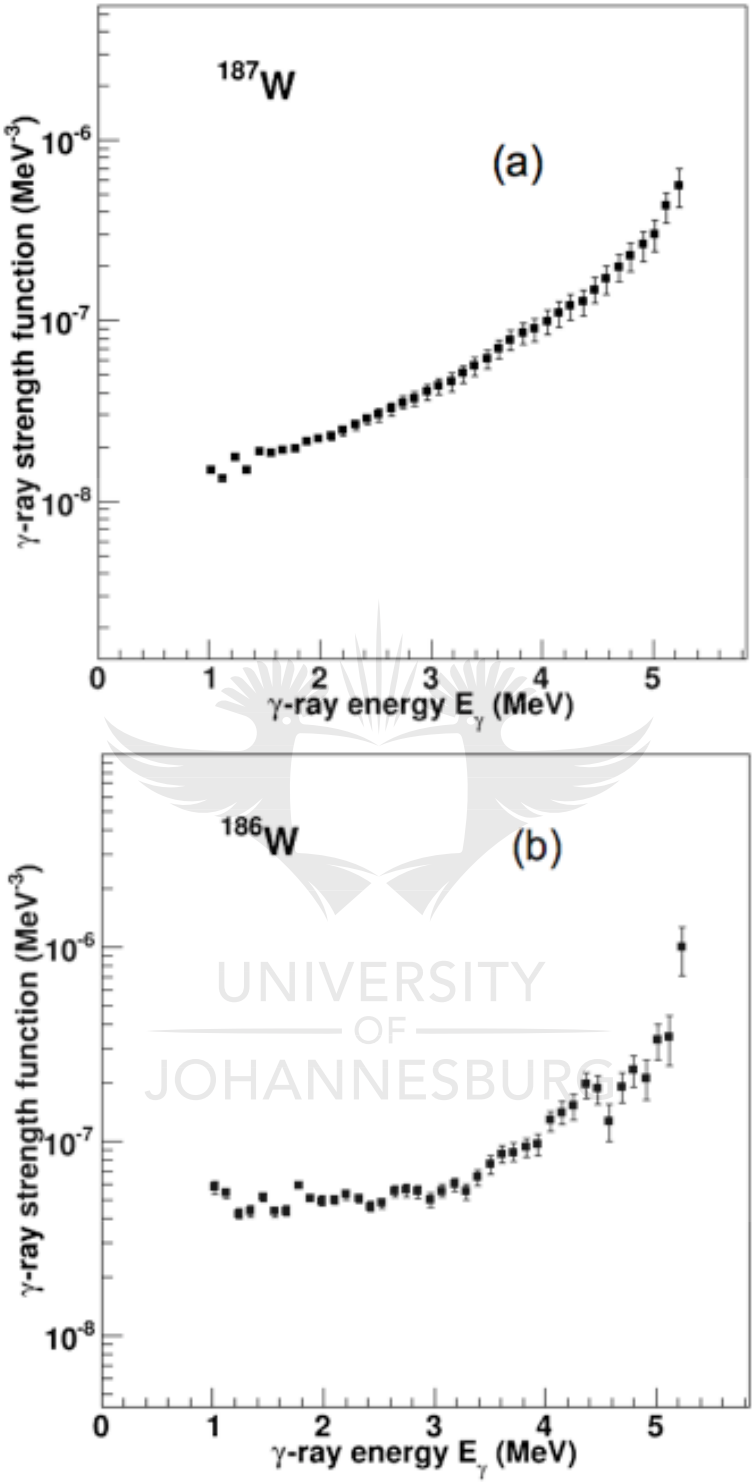

Figure 4.18: The normalized γ strength function of ^{187}W (a) and ^{186}W (b).

Chapter 5

Discussion

The extracted NLD and γ-SF described in the previous chapter were used in Hauser-Feshbach formalism, used in the TALYS reaction code [12], to calculate the (n, γ) cross-sections constraints. These are obtained using the possible extreme values of NLD and γ-SF of the compound nuclei ^{186,187}W. These resulted from uncertainties in the D_0 and Γ_γ. Hence, the normalization of $\rho(E_x)$ with $D_0 + \Delta D_0$ and $D_0 - \Delta D_0$ yielded lower and upper errors-bars of $\rho(E_x)$, respectively. On the other hand the possible upper extreme values of the γ strength functions resulted from normalization using $D_0 - \Delta D_0$ and $\Gamma_\gamma + \Delta\Gamma_\gamma$, while the possible lower extreme values was obtained by normalizing with $D_0 + \Delta D_0$ and $\Gamma_\gamma - \Delta\Gamma_\gamma$. These error-bands are provided in figures 5.1 and 5.2 and the corresponding normalization quantities for both nuclei are also shown in Table 5.1.

isotope		D_0	Γ_γ	$E_0(MeV)$	T (MeV)
^{186}W	Upper	6.3	81.4	-0.826	0.546
	Lower	7.7	66.6	-0.826	0.546
^{187}W	Upper	91	58	-1.227	0.535
	Lower	107	44	-0.666	0.570

Table 5.1: Table for different combinations of D_0 and Γ_γ for calculating upper and lower cross section errors.

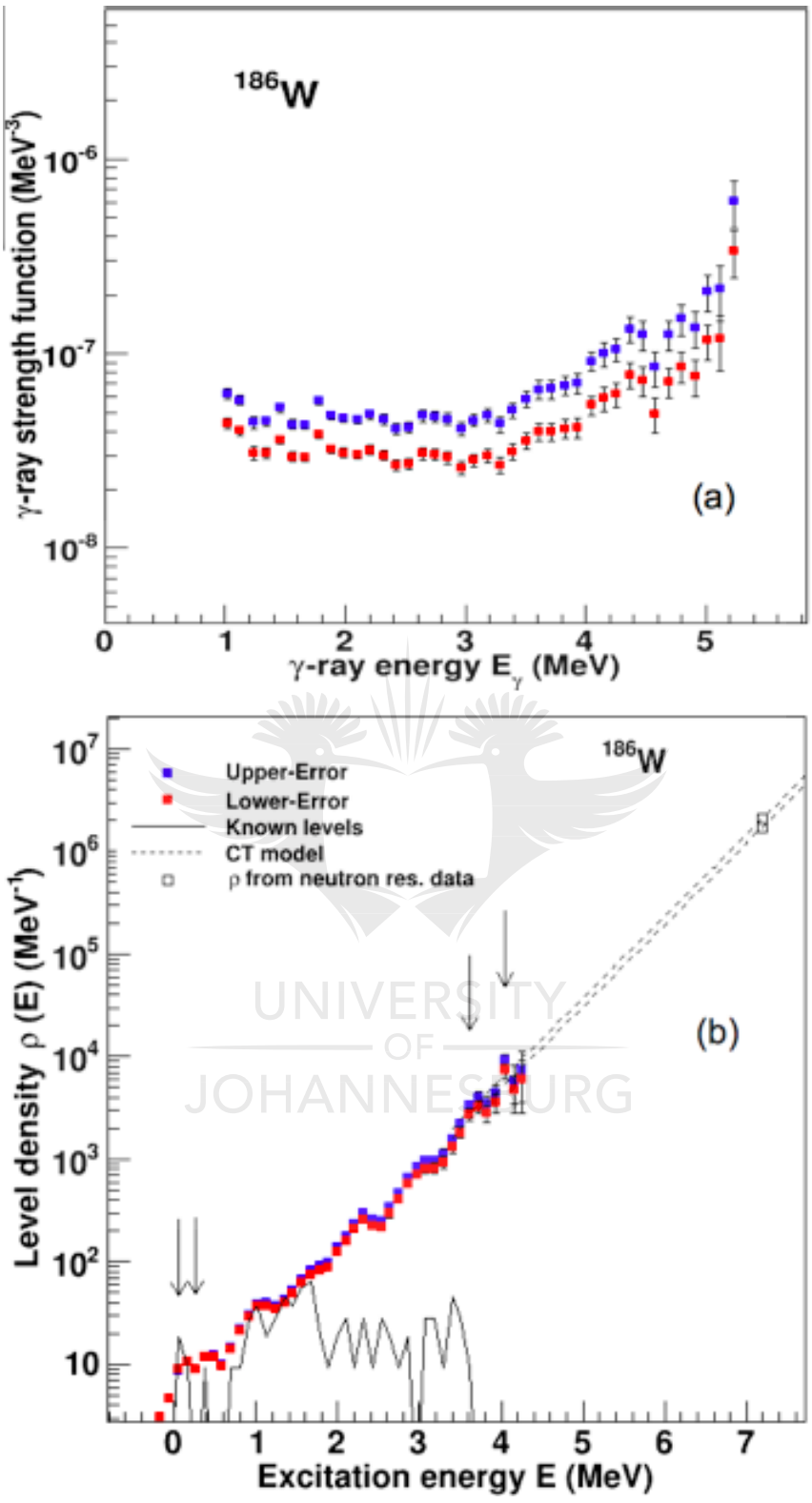

Figure 5.1: The γSF (a) and nuclear level density (b) error-bands of ^{186}W.

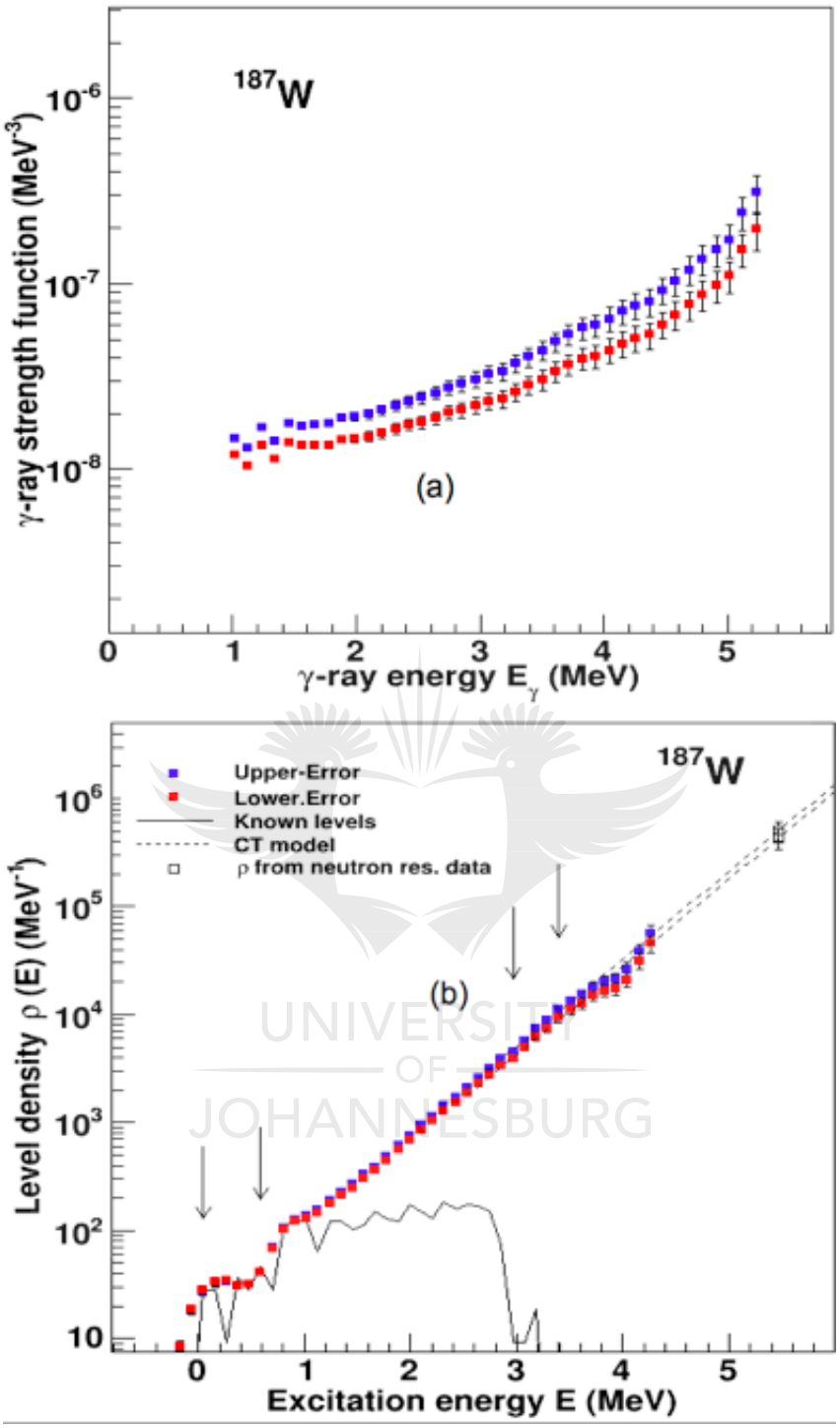

Figure 5.2: The γSF (a) and nuclear level density (b) error-bands of ^{187}W.

The resultant lower and upper extremes neutron capture cross section are provided in figures 5.3 (a) and 5.3 (b). The ^{186}W nucleus is stable and therefore

there exist experimental data from direct measurements obtained using the neutron time-of-flight (n-TOF) method. These are compared with the cross sections calculated in this work for ^{186}W and thus used as benchmark case for the present study. It is clear that most of the known data are well reproduced by the present experimentally constrained calculations (see figure 5.3 (a)), especially in the neutron energy range relevant for s-process (10-50 keV), providing confidence in the method and hence on the new ^{185}W(n,γ) cross sections (see figure 5.3 (b)). The known ^{186}W(n,γ) cross sections are available on EXFOR database [33] and are the experimental efforts of Refs. [34; 35; 36; 37]. It is observed that the data from [34] does not agree completely all the cross sections, however this is beyond the scope of this work but is worth looking into, in the future. The ^{185}W(n, γ) cross sections obtained in this study are first-ever experimentally constrained neutron capture cross section data for ^{185}W in the energy region relevant to s-process.

The (n, γ) cross sections for ^{185}W and ^{186}W can be useful in estimation of the reaction rate in hot stellar environments. This is where the target nucleus exists in thermally excited states and not confined to ground state. At such environments, the relative velocities v_T obey the Maxwell-Boltzmann distribution (MBD). Hence the reaction rate in hot stellar environments for neutron induced reactions can be obtained by integrating our neutron capture cross sections over the MBD of neutron energies. This step is one of the future plans of this project.

Futhermore, the γ-ray strength function(γSF) of ^{186}W shows an up-bend at $E_\gamma < 3$ MeV (see figure 4.18 (b)). Although the evolution of this feature in the nuclear chart has not been thoroughly investigated, but it has been observed in γ-SF of several nuclei (^{44,45}Sc, ^{50,51}V, $^{44-46}$Ti, ^{56,57}Fe, ^{93,98}Mo, ^{138}La, ^{74}Ge) [38; 39; 40; 41; 42; 43; 44], which were measured using Oslo method. Its existence in the Mo isotopes has also been independently confirmed with a model-

independent experimental approach, known as Ratio Method, by Ref. [45]. Although there is still no conclusive theoretical explanation for the up-bend but there are different theoretical efforts which have been able to reproduce it in nuclei where it has been already observed. For example according to Ref. [46] it may result from the reorientation of spins with high-j neutron and protons orbits giving M1 radiation, while Ref. [47] predicts that it may be caused by the single particle transition from quasi-continuum emitting E1 radiation. These were based on Shell model calculations and thermal continuum quasi-particle random phase approximation (see figures 5.4 and 5.5 for illustration). The ^{186}W isotope is currently the heaviest nucleus where the up-bend has been observed. There is no doubt that this structure should be further scrutinized experimentally to understand its physical origin, especially because it has been shown if it indeed exists in neutron rich nuclei, it can boost r-process reaction rates by up to 100 times [48; 49].

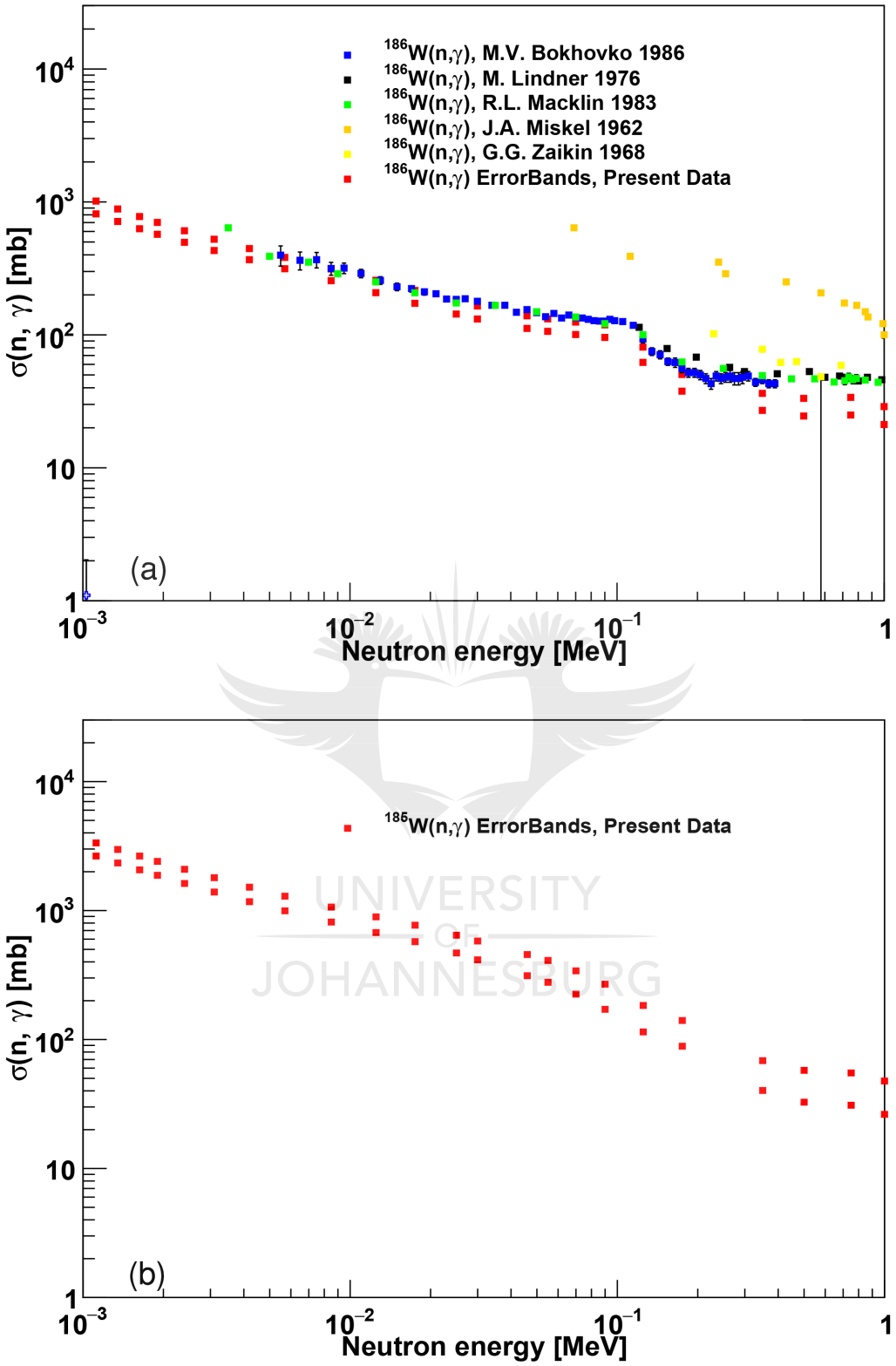

Figure 5.3: The (n, γ) cross sections for (a)^{186}W and (b) ^{185}W nucleus.

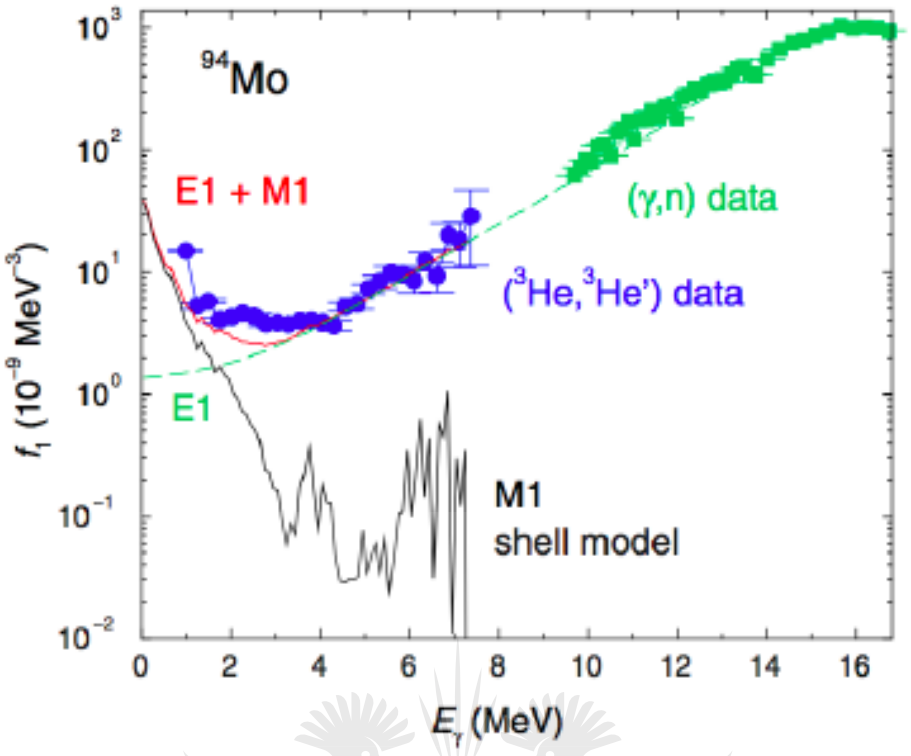

Figure 5.4: Experimental and theoretical γ strength function of ^{94}Mo [46].

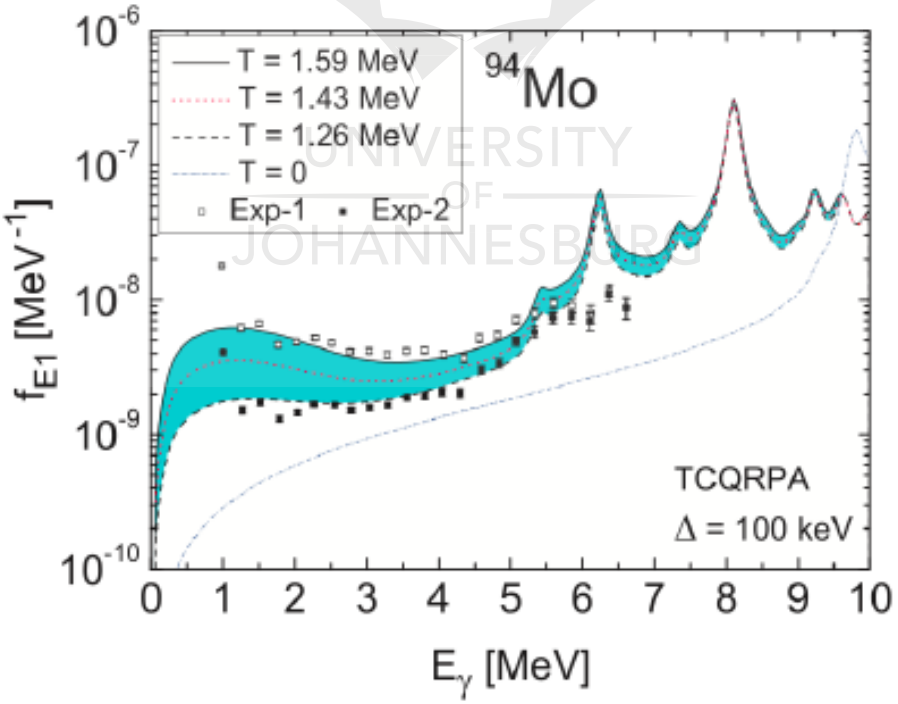

Figure 5.5: Experimental and theoretical γ strength function of ^{94}Mo [47].

Chapter 6

Summary and Future Outlook

In the s-process path there are certain locations with unstable nuclei which have neutron-capture and β-decay rates that are comparable in magnitude. These nuclei split the s-process into two branches and therefore are referred to as s-process branch points. They are of special interest because they can be used to determine the constraints of s-process temperature and neutron density in the asymptotic giant branch (AGB) stars. These quantitative analysis require high quality experimental neutron capture cross section data. However, such data cannot be obtained with direct measurements since it is impossible to make target material of these unstable nuclei. One of such branch points is ^{185}W which is not only important for constraining astrophysical conditions in the AGB stars, but it also plays a major role in the so-called Re-Os cosmochronology. However, it has been pointed out in the literature that the possible existence of s-process branching at ^{187}W induces complications in the quantitative interpretation of this cosmochronometer.

The ^{185}W(n,γ) cross sections has been successfully constrained within the Hauser-Feshbach model, using the experimental γ strength function and nuclear level density of ^{186}W nucleus. These statistical nuclear properties of ^{186}W were obtained using the ^{186}W(d,d') reaction. The data analysis was performed

using the Oslo method applied on charged particle- γ coincidence events. During the experiment, SiRi array was used charged particles detection, while γ rays were measured in the CACTUS multi-detector array. This indirect experimental method of constraining neutron-capture cross sections was also benchmarked by comparing the new ^{186}W(n,γ) cross sections, obtained in the present study, with various experimental data taken from literature. This comparison showed an excellent agreement, providing confidence in method and our extracted ^{185}W(n,γ) cross section data. The new obtained cross sections data will be included large network calculations in future, to reduce uncertainties that arise from s-process production of Os. Once enough data is taken from nuclei in s-process path, the contribution of s-process can be removed from Os giving better estimate in the β decay duration of Re.

Furthermore, the γ strength function of ^{186}W showed a low energy enhancement at $E_\gamma < 3$ MeV, and this is the heaviest nucleus where this structure has been observed. This confirms the hypothesis of Ref. [29] which says that an upbend is not confined within the nuclei with mass $A < 106$. Although there is no conclusive theoretical explanation for this low energy structure, it is vital to systematically investigate its extent in the neutron rich nuclei where it can significantly enhance r-process reaction rates. We are also planning to normalize the γ SF and NLD of ^{186,187}W using other spin distribution models such as the Hartree-Fock-Bogoliubov + Combinatorial (HFB+comb.) model. This is not expected to have a major effect on the neutron cross sections, as already shown by Ref. [29], but it will be checked before an attempt for publication of present results is made. Once this normalization with the (HFB+comb.) is completed the ^{185}W(n,γ) cross sections will be intergrated over the Maxwellian-distribution averaged cross sections of ^{185}W at the s-process temperature. Our Maxwellian averaged cross sections will also be compared with the work of Sonnabend et al [51].

Bibliography

[1] I. Thompson, F. Nunes *Nuclear Reactions for Astrophysics*, (Cambridge Universty Press, United Kingdom, 2009)

[2] Cameron, A. G. W. "NUCLEAR REACTIONS IN STARS AND NUCLEOGENESIS." Publications of the Astronomical Society of the Pacific, vol. 69, no. 408, pp. 201–222 (1957).

[3] E. M. Burbidge, G. R. Burbidge, W. A. Fowler, and F. Hoyle, Rev. Mod. Phys. 29, 547 (1957).

[4] Blaum, Klaus *et al.*, Contemp. Phys. 51, pp. 149-175 (2010).

[5] F. Kappeler *et al.*, Review of Modern Physics 83, 157 (2011).

[6] U. Abbondanno *et al.*, Phys. Rev. Lett. 93, 161103 (2004).

[7] D.D. Clayton, Astrophys J. 139, 637 (1964).

[8] J. W. Truran Proc. Natl. Acad. Sci. USA Vol. 95, pp. 18–21, (1998).

[9] T. Shizuma et al., Phys. Rev C 72, 025808 (2005).

[10] A. Schiller *et al.*, Nucl. Instr. and Meth. Phys. Res. A 447, 498 (2000).

[11] W. Hauser, H. Feshbach, Phys. Rev. 87, 366 (1952).

[12] A.J. Koning *et al.*, Nuclear Data for Science and Technology (EDP Sciences; eds O. Bersillon *et al.*), p. 211, (see also http://www.talys.eu) (2008).

[13] H.A. Bethe, Phys. Rev. 50, 332 (1936).

[14] A. Gilbert and A.G.W. Cameron, Can. J. Phys. 43, 1446 (1965).

[15] G. A. Bartholomew, E. D. Earle, A. J. Ferguson, J. W. Knowles, and M. A. Lone. Gamma-Ray Strength Functions, pages 229–324. Springer US, Boston, MA, . ISBN 978-1-4615-9044-6. doi: 10.1007/978-1-4615-9044-6 4. URL http://dx.doi.org/10.1007/ 978-1-4615-9044-6_4. (1973).

[16] M. Guttormsen *et al.*, Nucl. Instr. and Meth. Phys. Res. A 374, 371 (1996).

[17] M. Guttormsen *et al.*, Nucl. Instr. and Meth. Phys. Res. A 255, 518 (1987).

[18] D. M. Brink, Ph.D. thesis, Oxford University, pp. 101-110 (1955).

[19] www.nndc.bnl.gov.

[20] R. Capote et al., Reference Input Parameter Library, RIPL-2 and RIPL-3; available online at http://www-nds.iaea.org/RIPL-3/.

[21] A.C. Larsen *et al.*, Phys. Rev. C 83, 034315 (2011).

[22] J.A. Holmes *et al.*, Atomic data and nuclear data tables 18,305-412 (1976).

[23] A. C. Larsen, PhD thesis, University of Oslo, (2008).

[24] C. Iliadis, *Nuclear Physics of Stars*, (Wiley-VCH, Germany, 2015).

[25] A.-L. Manninen, CLINICAL APPLICATIONS OF RADIOPHOTOLUMINESCENCE (RPL) DOSIMETRY IN EVALUATION OF PATIENT RADIATION EXPOSURE IN RADIOLOGY Determination of absorbed and effective dose (2014).

[26] M. Guttormsen *et al.*, Nucl. Instr. and Meth. Phys. Res. A 648, 168 (2011).

[27] J. Kopecky and M. UHL, Phys. Rev. C. 41, 1941 (1990).

[28] J. Kopecky et al., Phys. Rev. C 47, 312 (1993).

[29] B. V. Kheswa *et al.*, Phys. Rev. C 95, 045805 (2017).

[30] A.C. Larsen *et al.*, Phys. Rev. C 87, 014319 (2013).

[31] S. Siem *et al.*, Phys. Rev. C 65, 044318 (2002).

[32] H. T. Nyhus *et al.*, Phys. Rev. C 85, 014323 (2012).

[33] https://www.nndc.bnl.gov/exfor/exfor.htm

[34] Zaikin, G.G., Korzh, I.A., Sklyar, N.T. *et al.*, At Energy 25, 1362 (1968).

[35] J. A. Miskel, K. V. Marsh, M. Lindner, and R. J. Nagle Phys. Rev. 128, 2717 (1962).

[36] M. Lindner, R. J. Nagle & J. H. Landrum,. Neutron Capture Cross Sections from 0.1 to 3 MeV by Activation Measurements, Nuclear Science and Engineering, 59:4, pp. 381-394 (1976).

[37] R. L. Macklin, D. M. Drake & E. D. Arthur,. Neutron Capture Cross Sections of 182W, 183W, 184W, and 186W from 2.6 to 2000 keV, Nuclear Science and Engineering, 84:2, pp. 98-119 (1983).

[38] A.C. Larsen *et al.*, Phys. Rev. C 76, 044303 (2007).

[39] A.C. Larsen *et al.*, Phys. Rev. C 73, 064301 (2006).

[40] A.C. Larsen *et al.*, Phys. Rev. C 85, 014320 (2012).

[41] N.U. H. Syed *et al.*, Phys. Rev. C 80, 044309 (2009).

[42] M. Guttormsen *et al.*, Phys. Rev. C 83, 014312 (2011).

[43] A.C. Larsen *et al.*, Phys. Rev. Lett. 111, 242504 (2013).

[44] M. Guttormsen *et al.*, Phys. Rev. C. 71, 044307 (2005).

[45] M. Wiedeking *et al.*, Phys. Rev. Lett. 108, 162503 (2012).

[46] R. Schwengner *et al.*, Phys. Rev. Lett. 111, 232504 (2013).

[47] E. Litvinova & N. Belov , Phys. Rev. C. 88, 031302(R) (2013).

[48] T. Renstrøm *et al.*, Phys. Rev. C 93, 064302 (2016).

[49] A.C. Larsen *et al.*, Phys. Rev. C 82, 014318 (2010).

[50] B. V. Kheswa, PhD thesis, University of Stellenbosch, (2014).

[51] Sonnabend *et al.*, Astrophys. J. 583, pp. 506-513, (2003).